Exploring aerosol-cloud interactions in liquid-phase clouds over eastern China and its adjacent ocean using the WRF-Chem-SBM model

Jianqi Zhao[1], Xiaoyan Ma[1], Johannes Quaas[2], Hailing Jia[3]

[1]Key Laboratory for Aerosol-Cloud-Precipitation of China Meteorological Administration, Nanjing University of Information Science & Technology, Nanjing 210044, China
[2]Institute for Meteorology, Leipzig University, Leipzig, Germany
[3]SRON Netherlands Institute for Space Research, Niels Bohrweg 4, 2333 CA Leiden, the Netherlands

Correspondence to: Xiaoyan Ma (xma@nuist.edu.cn)

Abstract. This study aims to explore aerosol-cloud interactions in liquid-phase clouds over eastern China (EC) and its adjacent ocean (ECO) in winter based on WRF-Chem-SBM model which couples a spectral-bin cloud microphysics (SBM) and online aerosol module (MOSAIC) as well as the four-dimensional assimilation approach. The model evaluation demonstrates that data assimilation has an overall positive impact on the simulation, ~~and with its support,~~ so the model generally reproduces the observed meteorological fields, aerosol, and cloud parameters~~a predominantly favorable impact on the simulation, and the model reasonably reproduces the satellite-retrieved cloud parameters~~. Differences in meteorological, aerosol, and topographic ~~and aerosol~~ conditions lead to the discrepancies~~fferences~~ of ~~in EC and ECO~~ aerosol-cloud processes between~~in~~ EC and ECO, and thus ~~resulting in~~ induce ~~.~~ ~~higher numbers but lower sizes of~~ more and smaller cloud droplets in EC, and relatively ~~fewer numbers but more large droplets of~~ less but large cloud droplets in ECO. Statistical analyses ~~of model samples at each time and vertical layer~~ show that cloud droplet number concentration (N_d) increases and then decreases with aerosol number concentration (N_{aero}) in both EC and ECO, with the difference that the strong surface effects (surface longwave radiation cooling and terrain uplift) and intense updraft in EC ~~still~~ produce some high N_d at high N_{aero}, while the abundant water vapor in ECO ~~enables its~~ induce N_d to increase faster at low N_{aero} but the production of cloud droplets is suppressed at high N_{aero}. In precipitating clouds, cloud liquid water content (CLWC) increases with N_d and its increase rate gradually slows down, while in non-precipitating clouds, CLWC increases first and then decreases. Compared to ECO, EC is able to produce higher N_d and CLWC under abundant aerosol and supersaturation produced by multiple strong surface and atmospheric processes, and its inflection point N_d value at which CLWC begins to decrease in non-precipitating clouds is also higher. For aerosol-cloud relationship analyses, especially for samples over short time periods, column-based (vertical integration of the layers with liquid-phase clouds) statistics are less detailed and immediate than those based on individual vertical layers due to the inability to accurately match parameters based on the intensity of aerosol-cloud processes in each vertical layer and the effects of processes such as precipitation. Meteorological conditions suitable for EC cloud development include (1) moist air brought by strong easterly winds, (2) cooling and topographic uplift caused by strong northerly winds, and (3) strong updrafts.

Meteorological conditions suitable for ECO cloud development include (1) aerosol-rich and not excessively dry airflow from moderate westerly wind, (2) cooling caused by northerly winds, and (3) updrafts. Compared to EC, ECO cloud development is more limited by cooling and humidification due to atmospheric motion (surface effects and intense updraft in EC enable aerosol activation to occur also in the presence of significant warming or humidity reduction), while the higher water vapor content enables its high N_d to N_{aero} ratio (characterizing the intensity of aerosol activation) and CLWC to N_{aero} ratio (characterizing the speed of cloud development) to occur at higher temperatures than those of EC. High CLWC to N_{aero} ratio appears under similar meteorological conditions to high N_d to N_{aero} ratio, while it occurs more often at low N_{aero} conditions compared to moderate N_{aero} conditions where high N_d to N_{aero} ratio appears. ~~Multiple atmospheric supersaturation pathways and abundant aerosols in EC enable more aerosols to be activated, but limited water content makes them difficult to grow into large droplets. While atmospheric supersaturation pathway and aerosol number concentration (N_{aero}) limit the cloud droplet number concentration (N_d) in ECO, the relatively abundant water content enables more large cloud droplets to exist here. EC and ECO cloud liquid water content (CLWC) exhibit close variation trends with N_d, but differences in aerosols, supersaturation pathways, and water vapor conditions result in distinctions in CLWC variations and the differentiation between precipitation and non-precipitation clouds in the two regions. Meteorological conditions suitable for EC cloud development include (1) weak winds and strong surface radiative forcing cooling, (2) moist air brought by strong easterly winds, (3) cooling and topographic uplift caused by strong northerly winds, and (4) strong updrafts. Meteorological conditions suitable for ECO cloud development include (1) aerosol-rich and not excessively dry airflow from moderate westerly wind, (2) cooling caused by northerly winds, and (3) updrafts. In general, the effect of cooling on aerosol activation is more pronounced compared to humidification in EC and ECO. Moreover, the aerosol conditions suitable for aerosol activation and CLWC increase are similar overall, with the difference being that aerosol activation is strongest under moderate N_{aero} conditions, whereas high CLWC to N_{aero} ratios are often seen under low N_{aero} conditions in addition to moderate N_{aero} conditions.~~

1 Introduction

Atmospheric aerosols have significant effects on the Earth's radiation balance, water cycle, and climate system through direct absorption and scattering of solar radiation as well as indirect effects on cloud formation and development by acting as cloud condensation nuclei (CCN) and ice nuclei (IN) (Carslaw et al., 2010; Wilcox et al., 2013; Tian et al., 2021). The latter, known as the aerosol indirect effect, or more recently by the Intergovernmental Panel on Climate Change (2013) defined as effective radiative forcing due to aerosol-cloud interactions, RF_{aci}, remains a challenging scientific topic in climate assessment and prediction because of its complex mechanisms and high uncertainties (Church et al., 2013; Jia et al., 2019a; Arias et al., 2021). Liquid-phase clouds offer great opportunities to untangle aerosol indirect effect due to their sheer abundance and impact on cloud radiative forcing (Christensen et al., 2016).

Twomey (1977) pointed out that under a constant cloud water content, the activation of atmospheric aerosol particles entering into clouds leads to an increase in cloud droplet number concentration (N_d), a decrease in droplet size, and an increase

in cloud albedo. This mechanism, termed the aerosol first indirect effect, is revealed to be the key driver of aerosol indirect effect, besides, the rapid adjustments also contribute significantly (Quaas et al., 2020). Two key competing mechanisms exist in the latter, one of which is that an increase in N_d causes a decrease in precipitation efficiency and with this, a co-increase in cloud liquid water path (CLWP) and cloud fraction (CF), this mechanism dominates in precipitation clouds (Albrecht, 1989). The other mechanism dominates in non-precipitating clouds, i.e., with limited water content, the decrease in droplet size reduces sedimentation velocity and increases cloud-top liquid water content, resulting in additional cloud top cooling and pushing further entrainment and evaporation (Bretherton et al., 2007). Moreover, as cloud droplets decrease in size, their ratio of surface area to volume is higher and evaporation is faster, resulting in further enhancement of the negative buoyancy at cloud top (Small et al., 2009). Numerous studies have been conducted to assess the contribution of these three mechanisms. Statistical analysis based on satellite-retrieved data indicates that the CLWP of marine low clouds exhibits a weak decreasing trend with rising N_d caused by aerosol increase (Michibata et al., 2016; Rosenfeld et al., 2019). Gryspeerdt et al. (2019) found that CLWP is positively correlated with N_d at low N_d and droplet size greater than the precipitation threshold, i.e., delayed precipitation leads to increased CLWP. In contrast, for the clouds with high N_d and low possibility of precipitation, CLWP shows a negative correlation with N_d. In this case, the increase of aerosol leads to the decrease of cloud droplet size and the increase of N_d, which in turn accelerates the mixing and evaporation process and makes CLWP decrease. The CLWP response to aerosols differs clearly between precipitation and ~~non precipitation~~non-precipitating clouds because of the significant influence of precipitation process on CLWP (Christensen and Stephens, 2012). CLWP has a significant positive correlation with the aerosol index (AI) in precipitation clouds, and the opposite in ~~non precipitation~~non-precipitating clouds (Chen et al., 2014). Furthermore, the response of CLWP to aerosol highly depends on meteorological conditions. Chen et al. (2014) indicated that CLWP and aerosol concentration show a negative correlation when entrainment mixing exerts a marked impact on the cloud-side evaporation process (which usually occurs under free troposphere with dry and unstable atmosphere), and this relationship shifts to positive as the atmosphere becomes moist and stable. Such statistical analysis, however, suffers severely from retrieval uncertainties (Arola et al., 2022). In turn, also "opportunistic experiments" such as the analysis of ship and pollution tracks hint at a decrease in CLWP but an increase in cloud horizontal extent in response to aerosol increases (Toll et al., 2019; Christensen et al., 2022). In spite of considerable efforts in recent researches to unravel aerosol-cloud interactions, it remains challenging to distinguish and quantify underlying mechanisms of aerosol-cloud interactions under diverse air pollution and meteorological conditions.

In order to further resolve the mechanisms of aerosol-cloud interactions, the proper use of numerical simulations is necessary. Current global climate models (GCMs) have difficulties in accurately representing the response of cloud to aerosol, which is mainly due to (1) the limitation of coarse model resolution, (2) the absence of sufficient consideration of cloud droplet spectral characteristics, and (3) the fact that most current GCMs parameterize the precipitation mechanism through the autoconversion process as an inverse function of N_d, without accurate representation of entrainment-mixing processes (Quaas et al., 2009; Bangert et al., 2011; Michibata et al., 2016; Zhou and Penner, 2017). Regional climate models (RCMs) with higher resolution and finer physical parameterization can effectively compensate for at least some of these shortcomings and better

reproduce the physical processes, which help to further distinguish and quantify the aerosol-cloud interaction mechanisms (Li et al., 2008; Bao et al., 2015). The Weather Research and Forecasting model (WRF) has been widely used in regional numerical simulation studies because of its advanced technology in numerical calculation, model framework, and program optimization, which has many advantages in portability, maintenance, expandability, and efficiency (Maussion et al., 2011; Islam et al., 2015; Xu et al., 2021). The chemistry-coupled version of the WRF model (WRF-Chem) allows to simulate the spatial and temporal distributions of reactive gases and aerosol, spatial transport and their interconversion while simulating meteorological fields and atmospheric physical processes (Tuccella et al., 2012; Sicard et al., 2021). Bulk and bin approaches are commonly utilized to simulate regional cloud microphysical processes. Bulk schemes diagnose the size distribution of hydrometeor based on different predicted bulk mass (one-moment schemes) or number and mass mixing ratios (double-moment schemes) and assumed size distribution, showing significant limitations in reproducing processes such as condensation, deposition and evaporation (Lebo et al., 2012; Wang et al., 2013; Fan et al., 2015). Bin schemes predict the size distribution of hydrometeors based on a number of discrete bins, enabling better representation of cloud microphysical processes. As stated by Khain et al. (2015), previous studies have demonstrated that bin schemes outperform bulk schemes in simulations. The evaluation of WRF-chem cloud microphysics by Zhang et al. (2021b) also showed that the bin scheme using the explicit approach reproduced the aerosol-induced convection and precipitation enhancement that the bulk scheme using the saturation-adjusted approach failed to model. In this study, the WRF-Chem-SBM model (Gao et al., 2016) is used, in which the Model for Simulating Aerosol Interactions and Chemistry (MOSAIC) in WRF-Chem (Fast et al., 2006) is coupled with a spectral-bin microphysics (SBM) scheme (Khain et al., 2004). In WRF-Chem-SBM, aerosol information is provided for cloud microphysical simulations, and cloud microphysical parameters are offered to aerosol-chemistry simulations, which are of great help to reproduce accurate aerosol and cloud conditions as well as to distinguish and quantify aerosol-cloud interaction mechanisms.

Eastern China (EC) is one of the most human-active regions worldwide, resulting in numerous anthropogenic aerosol emissions. The contrast between the high aerosol-content air masses of EC and the relatively clean air masses of the Pacific Ocean makes EC and its adjacent ocean (ECO) ideal regions for exploring aerosol-cloud interactions (Fan et al., 2012; Wang et al., 2015; Zhang et al., 2021a). It is shown that low clouds contribute the most to the Earth's energy balance due to their broad coverage and the albedo effect governing their impact on emitted thermal radiation (Hartmann et al., 1992). The statistics of Niu et al. (2022) using the satellite data from 2007-2016 show that low clouds in EC and ECO occur most frequently in winter, reaching more than 50%, with stratocumulus clouds, which are persistent and sensitive to aerosol variations (Jia et al., 2019b), constituting more than 70% of the low clouds. Therefore, the EC and ECO aerosol-cloud response in winter is an ideal condition to investigate aerosol-cloud interactions in liquid-phase clouds. Based on the WRF-Chem-SBM model, we investigate the aerosol-cloud interaction mechanisms of EC and ECO in winter by obtaining detailed and high-resolution aerosol, cloud parameters as well as meteorological information through reproduction of real scenarios.

The paper is structured as follows: Section 2 introduces the model configuration and observational data used in the study, Section 3 presents the evaluation of simulated results and the analysis of aerosol-cloud responses presented in the simulations, and the summary is given in Section 4.

2 Methods and Data

2.1 Simulation Setup

We performed model simulations using the WRF-Chem-SBM (Gao et al., 2016), in which. In this model, the 4-bin MOSAIC

135 aerosol module treats mass and number of nine major aerosol species, including sulfate, nitrate, sodium, chloride, ammonium, black carbon, primary organics, other inorganics, and liquid water (Zaveri et al., 2008). The diameters of 4 bins ranges from 0.039-0.156, 0.156-0.624, 0.624-2.5 and 2.5-10.0 μm, respectively, and aerosol particles are assumed to be internally mixed. This module is capable of treating processes such as emissions, new particle formation, particle growth/shrinkage due to uptake/loss of trace gases, coagulation, dry and wet deposition (Sha et al., 2019). In addition, this model incorporates the fast

140 version of SBM, which solves a system of prognostic equations for three hydrometeor types (liquid drops, ice/snow and graupel) and CCN size distribution functions (Khain et al., 2010). Each size distribution is structured by 33 mass doubling bins (i.e., the mass of the particle in the kth bin is twice that of the k-1th bin). The cloud microphysical processes described in the SBM contain aerosol activation, freezing, melting, diffusion growth/evaporation of liquid drops, deposition/sublimation of ice particles, drop and ice collisions.

145 The model domain is shown in Fig. 1, andwhere two sets of two-layer nested grids are employed. The parent domainouter grids (12 km resolution) have centroids and grid points of (32°N, 120°E) and 151 × 125, while the nested domainsinner grids (4 km resolution) represent EC (160 × 160 grid points) and ECO (121 × 121 grid points), respectively. There are 48 vertical layers up to 50 hPa, with layer spacing extending from 40 m near the surface to 200 m at 3000 m altitude and over 1000 m above 10000 m altitude. The simulations run from 00:00:00 UTC on 1 Feb 2019 to 00:00:00 UTC on 13 Feb 2019, where the

150 first 24 h are disregarded as spin-up and not involved in subsequent analyses. The model outputs once per hour. Meteorological initial and boundary conditions are obtained from the National Center for Environmental Prediction (NCEP) FNL global reanalysis data with 0.25° resolution and available every 6 h (https://rda.ucar.edu/datasets/ds083.3, last access: 11 October 2023), chemical initial and boundary conditions from Community Atmosphere Model with Chemistry (Emmons et al., 2020), and anthropogenic emission sources come from the Multi-resolution Emission Inventory for China (MEIC) 2016 version

155 developed by Tsinghua University (http://meicmodel.org.cn, last access: 19 March 2023). As presented in Fig.1, the anthropogenic aerosols of EC and ECO are dominated by EC under winter monsoon, although the model domain contains countries and regions other than China, MEIC can satisfy the anthropogenic aerosol simulation of the region concerned in this study. The model parameterization settings are listed in Table 1. Using these configurations, EC and ECO simulations require around 15,000 and 10,000 CUP core-hours, respectively.
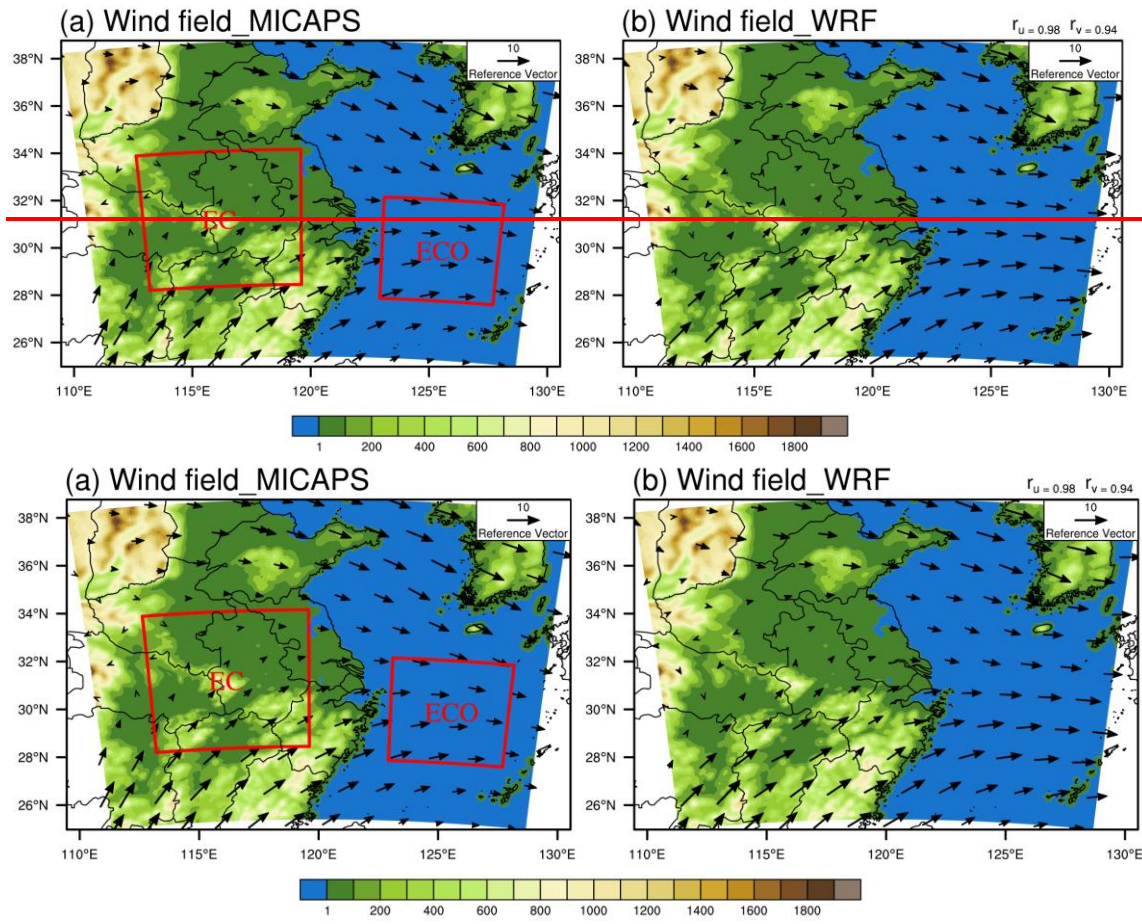
Figure 1. Topography (unit: m) of the model domain, MICAPS (a) and assimilated simulated (b) 850 hPa wind fields (unit: m·s⁻¹) during the simulation period and their correlation coefficients of u and v components (r_u、 r_v) given in the upper right corner

Table 1. Model parameterization settings

Process	Number	Name
Longwave radiation	4	RRTMG (Mlawer et al., 1997)
Shortwave radiation	~~3~~5	~~CAM~~ Goddard (Zhong et al., 2016)
Surface layer	1	MM5 Monin-Obukhov (Pahlow et al., 2001)
Land surface	2	Unified Noah (Chen et al., 2010)
Boundary layer	1	YSU (Shin et al., 2012)
Chemistry and aerosols	9	CBMZ and 4-bin MOSAIC (Sha et al., 2022)

Photolysis	2	Fast-J (Wild et al., 2000)
Sea salt emission	2	MOSAIC/SORGAM (Fuentes et al., 2011)
Dust emission	13	GOCART (Zhao et al., 2010)
Biogenic emission	3	MEGAN (Guenther et al., 2006)

2.2 Four-dimensional data assimilation

The accuracy of the meteorological field is crucial to reproduce realistic aerosol-cloud interaction ~~scenarios~~, and thus a four-dimensional data assimilation approach is used in both parent domain and nested domains ~~both parent domain and nested~~
180   ~~domains~~ to improve~~reduce the error of~~ the simulated meteorological field. This approach utilizes relaxation terms based on the model error at observational stations to make the simulated meteorological fields closer to reality (Liu et al., 2005), thus exerting positive effects on the simulation of atmospheric physical and chemical processes (Rogers et al., 2013; Li et al., 2016; Ngan and Stein, 2017; Zhao et al., 2020; Hu et al., 2022). The data used for assimilation are obtained from the NCEP operational global surface (https://rda.ucar.edu/datasets/ds461-0, last access: 19 March 2023) and upper-air
185   (https://rda.ucar.edu/datasets/ds351-0, last access: 19 March 2023) observation subsets, which contain meteorological elements such as altitude, wind direction, wind speed, air pressure, temperature and~~,~~ dew point ~~and relative humidity~~.

2.3 Observational data

We use multiple observational data ~~s~~ to assess ~~the impact of the four-dimensional assimilation and~~ the ability of the model to reproduce meteorological fields, aerosol and cloud parameters. Precipitation data is taken from the Integrated Multi-satellitE
190   Retrievals for GPM (IMERG)~~Global Precipitation Measurement (GPM) Level 3~~ dataset (Huffman et al., 2019) ~~((Huffman et al., 2019)https://disc.gsfc.nasa.gov/datasets/GPM_3IMERGDF_06/summary?keywords=Precipitation, last access: 30 May 2023)~~, of which the daily accumulated high quality precipitation product (0.1° resolution) is used in this study (https://disc.gsfc.nasa.gov/datasets/GPM_3IMERGDF_06/summary?keywords=Precipitation, last access: 30 May 2023). Other meteorological variables~~elements~~ are obtained from the Meteorological Information Comprehensive~~Combine~~ Analysis
195   and Process System (MICAPS) developed by the National Meteorological Center (NMC) of China (http://www.nmc.cn, last access: 19 March 2023), with 12 h temporal resolution and 11 vertical layers, containing meteorological elements such as wind field, height, temperature and temperature dew point difference. Near-surface $PM_{2.5}$ data are obtained from the National Urban Air Quality Real-time Release Platform of China National Environmental Monitoring Centre with 1 h temporal resolution (https://air.cnemc.cn:18007, last access: 19 March 2023). The cloud optical depth (AOD) data is obtained from the Moderate
200   Resolution Imaging Spectrometer (MODIS) MOD04_L2 dataset (Levy et al., 2015), of which the AOD product combining the "Dark Target" and "Deep Blue" algorithms with 10km resolution is used in this study (https://ladsweb.modaps.eosdis.nasa. gov/search/order/1/MOD04_L2--61, last access: 19 March 2023). The cloud parameters including cloud droplet effective

radius (CER), cloud optical thickness (COT), CLWP and cloud phase data at 1 km resolution, as well as cloud top temperature (CTT) at 5 km resolution (https://ladsweb.modaps.eosdis.nasa.gov/search/order/1/MOD06_L2--61, last access: 19 March 2023), are obtained from the MODIS Level-2 Cloud (MOD06_L2) product (Platnick et al., 2015) ~~(https://ladsweb.modaps.eosdis.nasa.gov/search/order/1/MOD06_L2--61, last access: 19 March 2023), from which we select cloud droplet effective radius (CER), cloud optical thickness (COT), CLWP and cloud phase data at 1 km resolution, as well as cloud top height (CTH),~~as well as ~~cloud top temperature (CTT) and cloud top pressure (CTP) at 5 km resolution (https://ladsweb.modaps.eosdis.nasa.gov/search/order/1/MOD06_L2--61, last access: 19 March 2023)~~. The CER, COT and CLWP are retrieved from 2.1 μm wavelength, which is the default value in the product (1.6 μm and 3.7 μm wavelength retrievals are also available).

Spatial correlation analysis (Pearson product-moment coefficient), Pearson linear correlation analysis, and root mean square error (RMSE) are used to assess the spatial and temporal correlations of the simulated and observed values as well as the error of the simulated values relative to the observations, respectively. To calculate these parameters, it is necessary to unify the spatio-temporal coordinates of the simulated and observed data. ~~In order to avoid evaluation uncertainties caused by the fact that low-resolution data do not contain small-scale information, the interpolation performed when comparing the model results with observations is from high resolution to low resolution.~~ Specifically, MODIS (1-10 km resolution) and IMERG (~~(~~0.1° resolution) data are interpolated to the WRF grid (12 km resolution) when comparing the model to satellite data, and WRF simulations~~data~~ are interpolated to the MICAPS grid (2.5° resolution) when comparing the model to MICAPS data. ~~We interpolate the observations into the same horizontal grid as the simulated data and interpolate the simulated data into the same vertical pressure layer as MICAPS when evaluating the meteorological field.~~

~~In addition, For~~ for the MODIS data, ~~we select the reliable~~ Some screening criteria~~criterion~~ are applied to MODIS-retrieved cloud variables~~cloud retrievals~~ to make sure liquid clouds are selected ~~according to the approach of(~~ (Saponaro et al., 2017), i.e., ~~:~~ (1) selecting only liquid-phase cloud parameters and (2) filtering out transparent-cloudy pixels (COT < 5) to limit uncertainties (Zhang et al., 2012). The same filtering also applied to WRF-Chem model results~~outputs~~ when we~~doing~~ evaluate~~ion~~ the simulations against MODIS data. ~~Since MODIS provides no information of~~ Cloud droplet number concentration N_d~~,~~ is calculated according to~~we refer to~~ the approach of Brenguier et al. (2000) and Quaas et al. (2006)~~utilizing MODIS COT and CER to calculate (when comparing the MODIS data, we did the same for the simulated values to obtain the simulated N_d, so that the two can be compared directly)~~:

$$N_d = \gamma \cdot COT^{0.5} \cdot CER^{-2.5} \tag{1}$$

where γ is an empirical constant with the value of 1.37×10^{-5} m^{-5}, and COT and CER are obtained from MODIS.~~.~~ Moreover, due to the discontinuity of MODIS data, we matched the simulated data with MODIS data in spatio-temporal coordinates for evaluation (i.e., the simulated value is valid only when the MODIS data is valid in that spatio-temporal coordinate, otherwise the simulated value is set as the missing and does not participate in the calculation). Due to the differences in satellite retrievals and model parameterization, the simulated liquid-phase clouds are often defined based on certain thresholds when comparing with satellite-retrieved data, e.g. Roh et al. (2020) classified the clouds with CLWC > 1 mg m^{-3} and cloud ice water content

(CIWC) < 1 mg m^{-3} as liquid-phase clouds. In this study, based on the selection of column COT ⩾ 5 that matched with MODIS filtering, the vertical layers (48 layers in total) with cloud optical thickness for water (COTW) > 0.1 and cloud optical thickness for ice (COTI) < 0.01 at each grid point and each time are selected as liquid-phase cloud layers, and the highest layer meeting
240   this condition is defined as the simulated cloud top (this filtering is only used for comparison with MODIS data, and the analysis of aerosol-cloud interactions in liquid-phase clouds in this study is strictly limited to CLWC > 0 and CIWC = 0).

3 Results and Discussion

3.1 Evaluation of ~~assimilation effect and~~ simulation result

Due to limitations in the resolution of observational data (e.g., MICAPS gridded upper-air meteorological field data with a
245   resolution of 2.5°) and data availability (e.g., only terrestrial near-surface observations of PM$_{2.5}$ are available), we utilized outer domain simulations when evaluating the model results. For aerosol-cloud analysis in Section 3.3 and beyond, we employed finer inner domain simulations.

Four-dimensional data assimilation directly impact~~alter~~s the simulations of meteorological field~~s~~ ~~simulation (such as~~
temperature, pressure, humidity and wind), ~~and thereby~~ ~~affects the~~ aerosol and cloud ~~simulation. We first examine the effect~~
250   ~~of assimilation to clarify whether assimilation brings more confidence to the study.~~ Figure 2 presents the vertical distribution of meteorological variables ~~,~~ from the simulations and observations ~~the simulated and observed meteorological elements before and after assimilation~~, as well as the RMSE and spatial correlation coefficients of the simulations~~simulated~~ relative to MICAPS observations at each layer. ~~The four-dimensional assimilation exerts slight effect on the height field (Fig. 2a), which is almost absent at the lower layers and exhibits slight increase at the upper layers in the RMSEs with respect to the observations~~
255   ~~compared to the unassimilated. In contrast to the height field, the assimilation presents significant improvements to the simulated temperature (Fig. 2b), and the RMSEs are effectively reduced by assimilation at all layers. The effects of assimilation on the temperature dew point difference (Fig. 2c) and wind v component (Fig. 2e) exhibit reduced low and high layer RMSEs and enlarged middle layer RMSEs, while the effects on wind u component (Fig. 2d) exhibit reduced low and middle layer RMSEs and enlarged high layer RMSEs.~~ As the complexity of atmospheric physical and chemical processes and data errors
260   resulted from processes such as observation and interpolation~~station data gridding~~, the assimilation exerts some positive effects on the simulated meteorological field, but also increases the difference between some of the simulated variables and the observations. Assimilation effectively improves the correlation between simulated and observed temperatures, dew point depression, middle level zonal wind, and meridional wind, while reducing the RMSE of simulated and observed temperatures, upper level dew point depression, and lower and upper level meridional winds. At the same time, however, it also weakens the
265   correlation between the simulated and observed low-level zonal winds, and increases the RMSE of the simulated and observed mid-level dew point depression, upper-level zonal winds, and mid-level meridional winds.~~effects revealed by the evaluation are not uniformly positive~~ But overall, the assimilation is positive and provides effective help in exploring aerosol-cloud

270
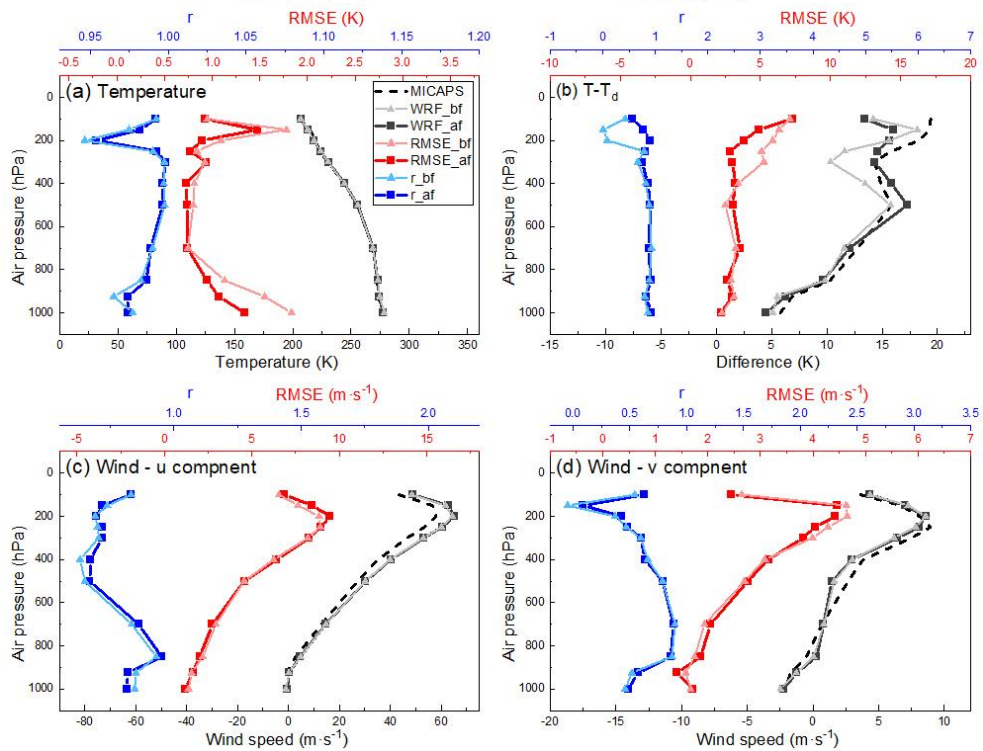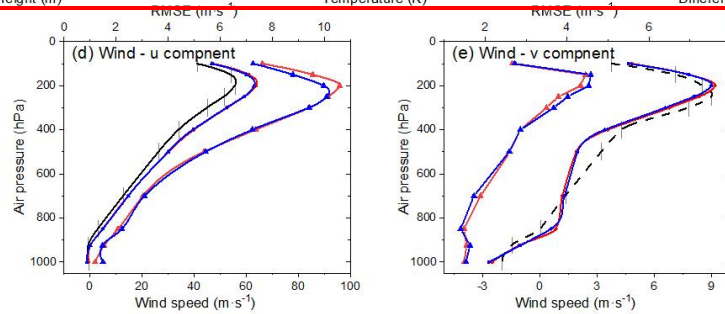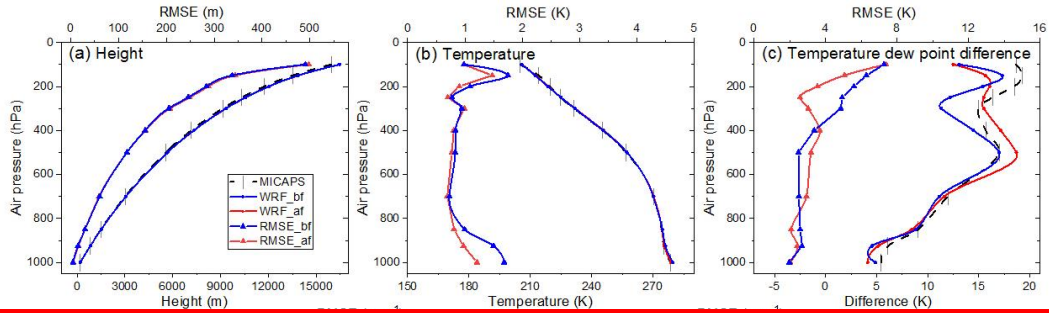
Figure 2. MICAPS and simulated average height (a), temperature (ba) and dew point depressiontemperature dew point difference (cb) as well as u (dc) and v (ed) components of wind during the simulation period (black lines) as well as RMSE (red lines) and spatial correlation coefficients (blue lines) between observations and simulations before and after assimilation for each vertical layer (subscripts " bf" and " af" represent simulation before and after assimilation)and their RMSE vertical distribution before (blue line) and after (red line) assimilation

As shown in Fig. 3, aAssimilation exerts indirect positive influences on precipitation, aerosol emission (mainly natural aerosols such as dust and sea salt), transport, and deposition. The RMSE of simulated and observed precipitation (Figs. 3a-c) is reduced by 61.50.4% after assimilation. In terms of aerosol spatial distribution (Figs. 3d-f), the model reasonably reproduces the MODIS AOD distribution, and there is no significant difference in the simulated average AOD before and after assimilation. To further evaluate the effect of assimilation on the simulation of aerosol temporal variationsAs reported by previous studies, the WRF-Chem simulated AOD (Fig. 3e-f) is underestimated compared to MODIS retrievals (Fig. 3d) due to the differences in obtaining methods and calculations, and this underestimation is clear in the low-value region (Kumar et al., 2014; Soni et al., 2018; Krishna et al., 2019). Overall, the model reasonably reproduces the MODIS AOD distribution, and after assimilation, the simulation matches better with MODIS retrievals, especially in EC and ECO regions near 30°N that are of concern in this study. The simulated and observed near-surface $PM_{2.5}$ distributions presented in Fig. 3g-i indicate that the simulated $PM_{2.5}$ before and after assimilation both reasonably reproduce the observed patterns, but the simulation without assimilation underestimates the $PM_{2.5}$ concentration. Supported by assimilation, the model better reproduces the meteorological field as well as atmospheric physical and chemical processes, thus effectively optimizing the aerosol simulation, with the RMSE between the simulated and observed near-surface $PM_{2.5}$ reduced from 35.22 µg m^{-3} to 27.73 µg m^{-3}. To evaluate the effect of assimilation on the simulation of $PM_{2.5}$ temporal variation, 16 stations with relatively continuous observation (Fig. 3h3a) are selected evenly from the model domain (Fig. 4). In general, the simulations before and after assimilation both reasonably reproduce the temporal variation of near-surface $PM_{2.5}$, and the correlation between simulated and observed $PM_{2.5}$ at all stations pass the test at 99% significance, whereas the simulations before assimilation overall underestimate the $PM_{2.5}$ concentration. But wWith assimilation, the simulated $PM_{2.5}$ concentrations are generally closer to the observations, and the correlation coefficients between the simulated and the observed have increased in 13 of the 16 stations, while the average correlation coefficient of the 16 stations has increased from 0.6348 to 0.5869.
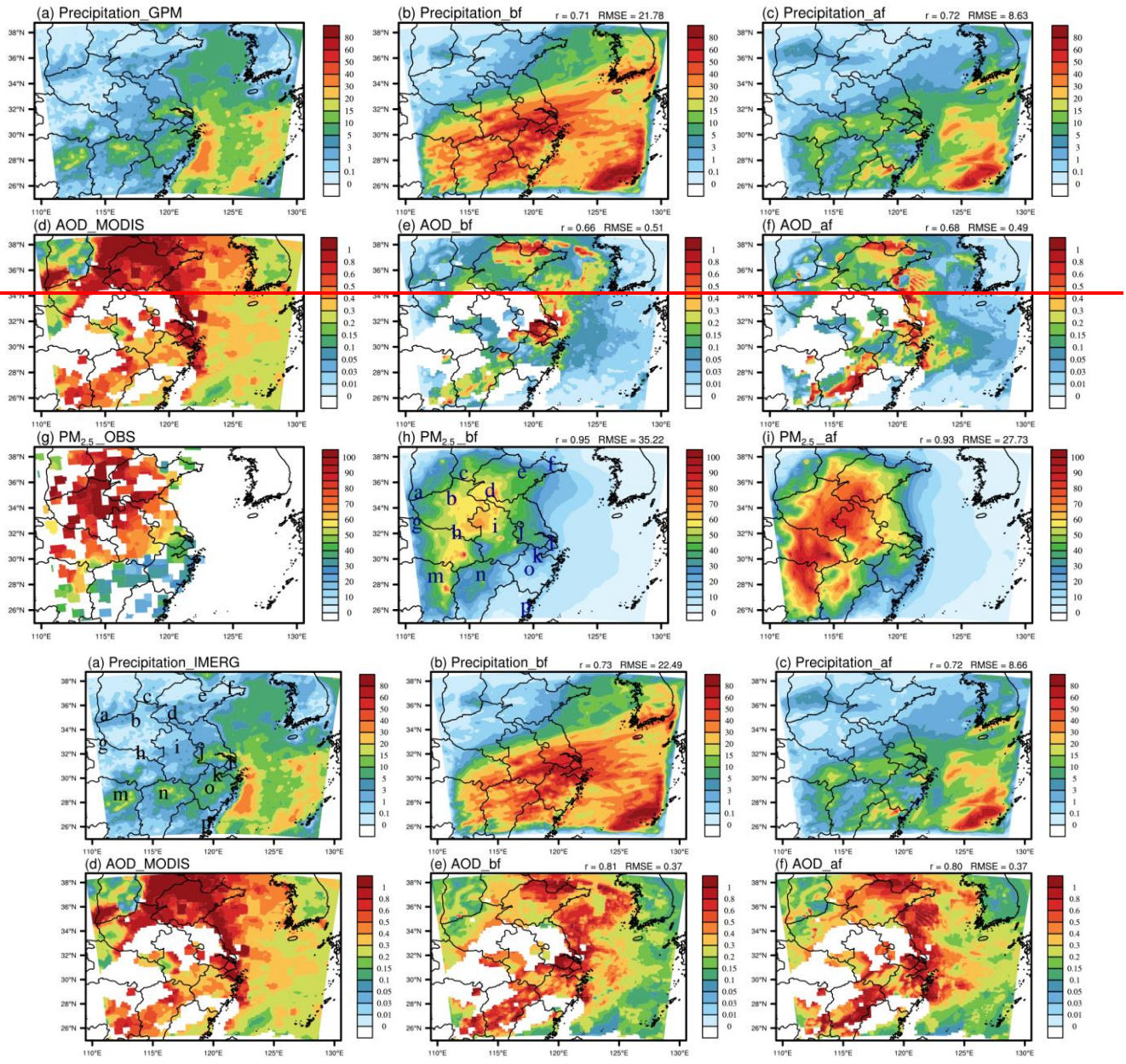
Figure 3. Distributions of accumulated precipitation (unit: mm, a-c~~),)~~ and average AOD (dimensionless, d-f) ~~and near-surface PM₂.₅ (unit: μg·m⁻³, g-i)~~ during the simulation period from the observation ~~(a, d and g)~~ as well as before ~~(b, e and h)~~ and after ~~(c, f and i)~~ assimilation of the meteorological fields (r and RMSE at the up-right corner represent the spatial correlation coefficient and root mean square error of the observed and the simulated, respectively, where RMSE is in the same unit as the variable in the figure. The subscripts " bf" and " af" in the subfigure captions have the same meaning as in Fig. 2. The markers

a-p in Fig. ~~3h~~ 3a represent the locations of the stations in Fig. 4)
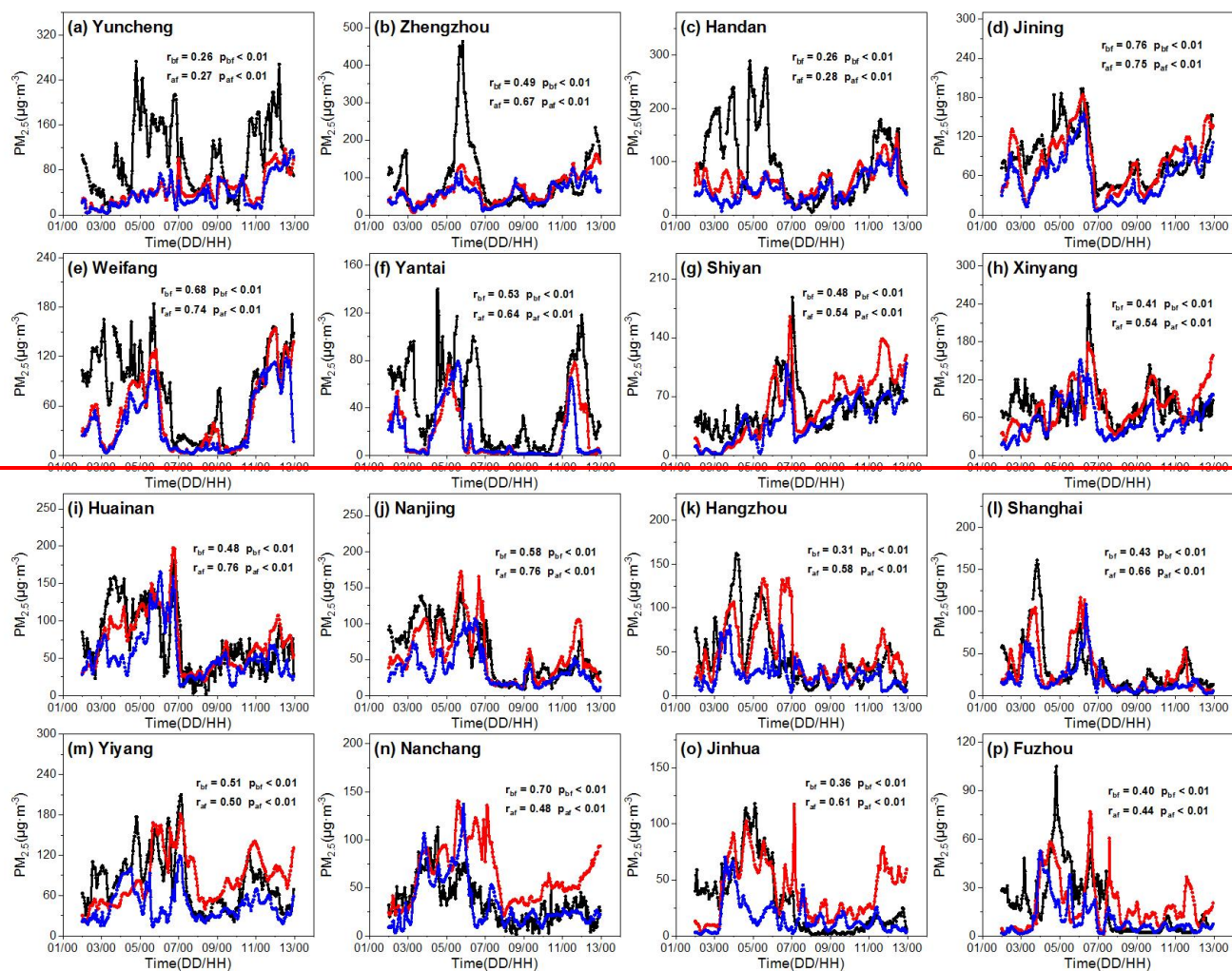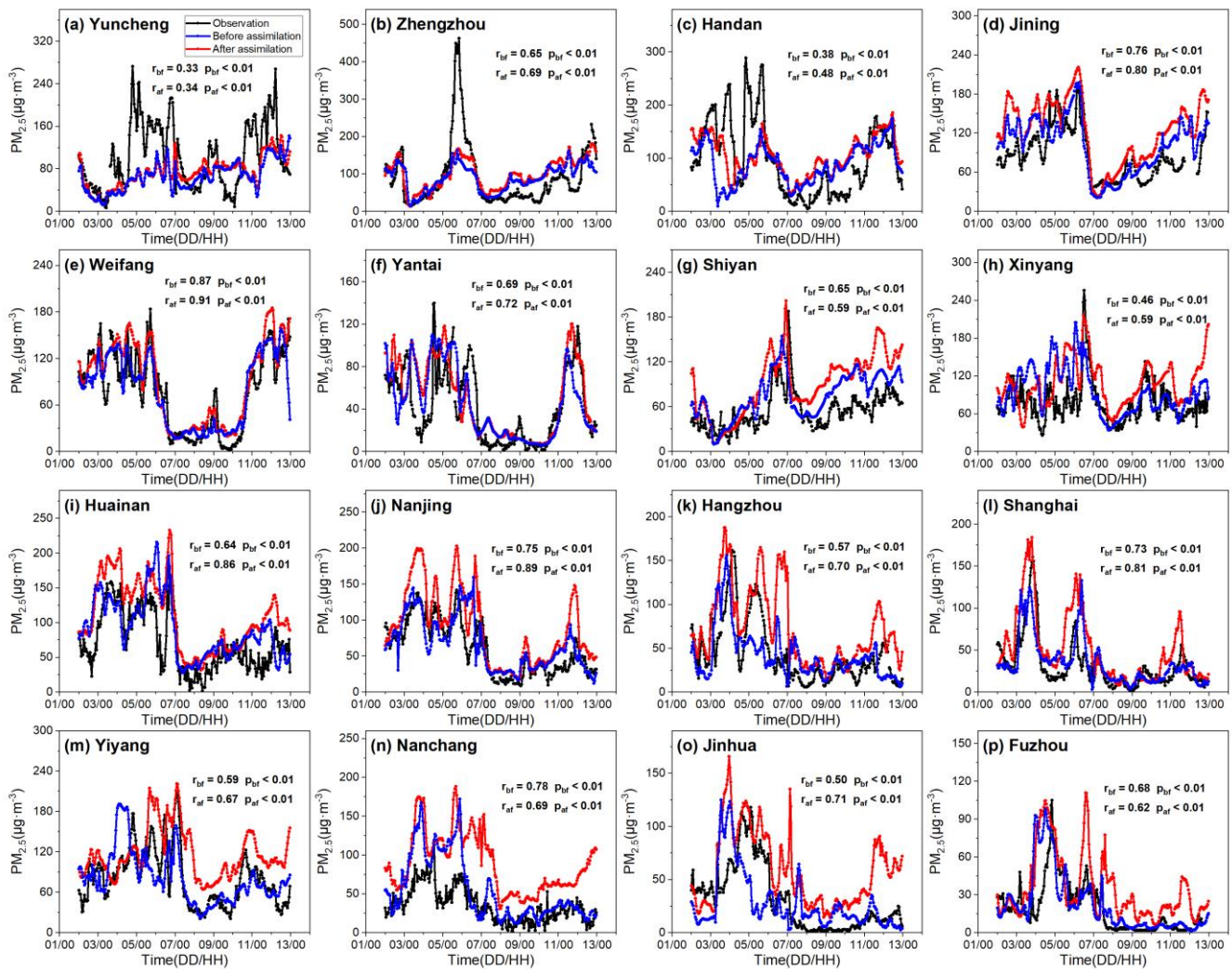
Figure 4. Temporal variations of near-surface $PM_{2.5}$ observed (black line) and simulated before (blue line) and after (red line) assimilation of meteorological fields, at each site~~.~~ ~~(The~~ the r and p values represent the correlation and significance of the observation and simulation, respectively, and subscripts "bf" and "af" have the same meaning as in the previous figure~~represent simulated before and after assimilation)~~

Figure 5 present~~illustrates~~ the simulated cloud parameters before and after assimilation and compared with~~to~~ MODIS~~data~~. It is~~can be~~ seen that the model without assimilation generally reproduces the spatial distribution of MODIS cloud parameters ~~before assimilation~~, but with some overestimation for~~of~~ CER and COT and some underestimation for~~of~~ N_d. Compared with MODIS, the simulation with assimilation produces overall higher N_d and lower CLWP over land but more reasonable CER and its distribution.~~Although assimilation makes the model produce some overestimation of continental N_d and some overestimation of CLWP, it effectively improves the simulation of the CER and makes the land sea distribution of cloud~~

320

325

~~droplet characteristics clearer and more plausible.~~ ~~For the CTT,~~ ~~T~~the model also reasonably reproduces the spatial distribution of ~~satellite~~ MODIS-retrieved~~al~~ COT and CTT, which is important to our analysis presented below. ~~south of 34°N, but does not simulate well north of 34°N. This is due to the fact that the model does not reasonably reproduce the aerosol distribution of this region (the MEIC inventory used in this study does not include anthropogenic emissions from Korea), satellite retrieval errors, and the difficulty of model parameterization to simulate such a cold liquid-phase cloud top (down to below -16°C), but it has little impact on the subsequent analyses because this region is not included in the EC and ECO that are of interest in this study.~~ ~~Figure 5 illustrates a comparison of cloud parameters between simulated and MODIS data. The model reasonably reproduces the spatial pattern of CER and N_d, i.e. low over land and high over ocean. Compared to MODIS, the model overestimates oceanic CER and underestimates oceanic N_d. Additionally, the model overall reasonably reproduces the values and distribution of CLWP, COT and cloud top parameters.~~
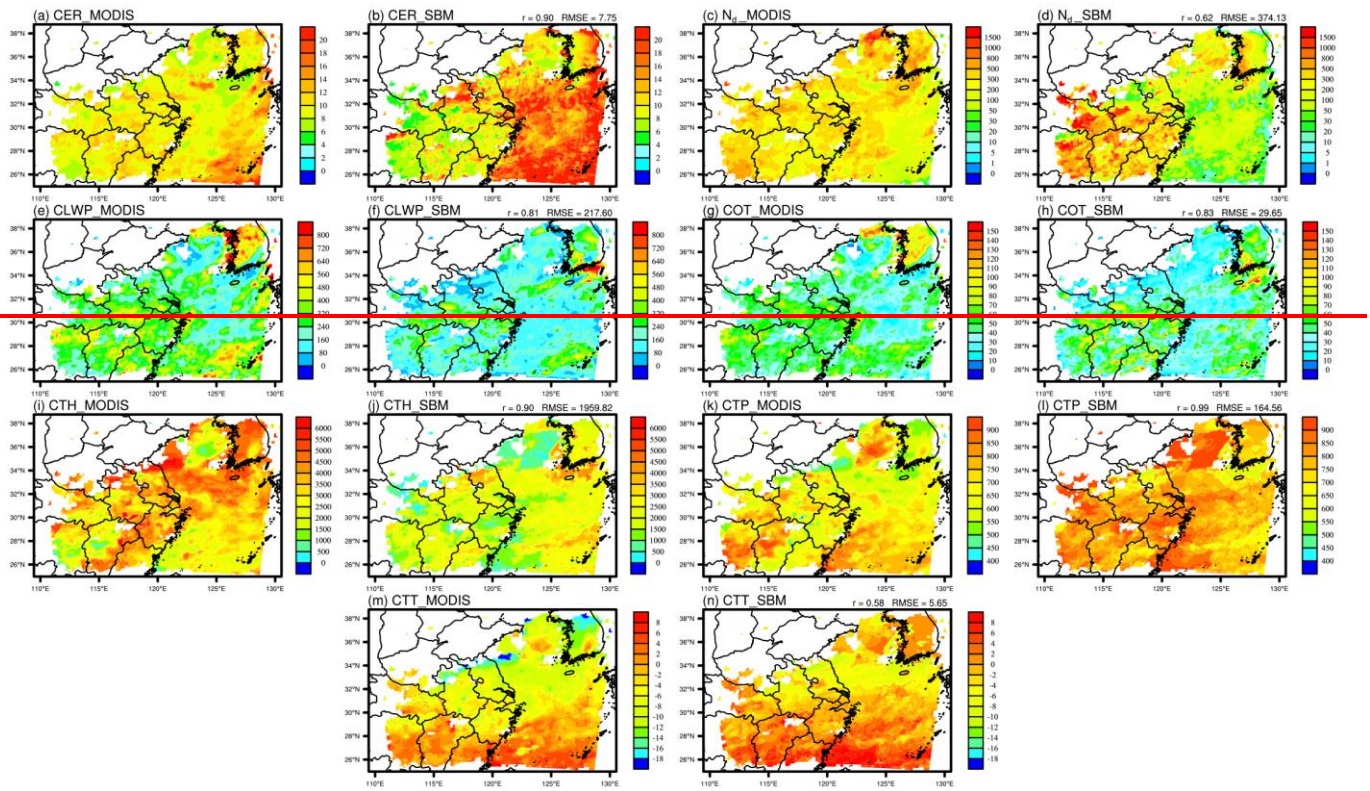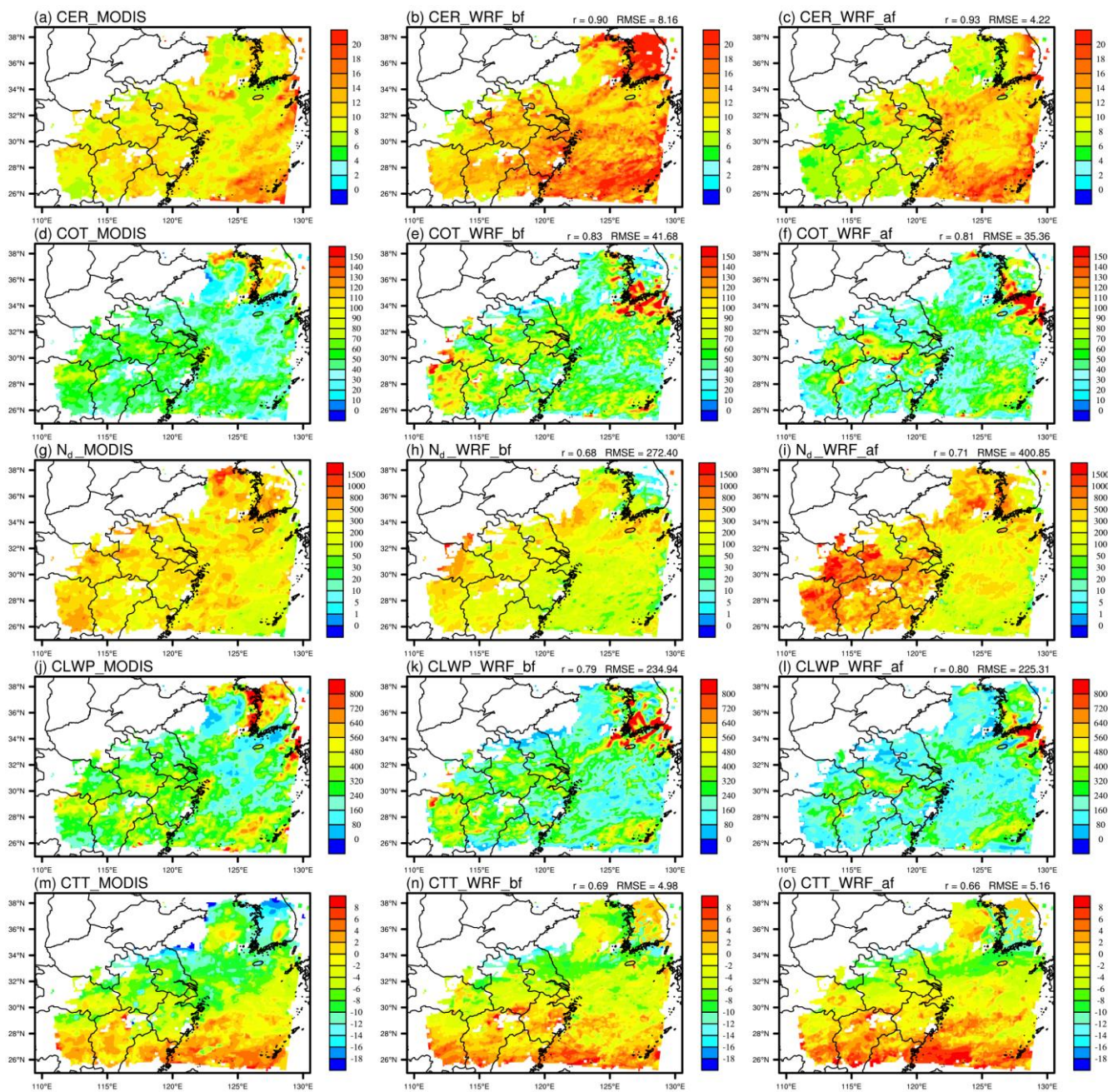
Figure 5. Spatial distribution of average CER (a-c, in μm), COT (d-f, dimensionless), N_d (g-i, in cm^{-3}), CLWP (j-l, in g·m^{-2}) and CTT (m-o, in °C) from MODIS and WRF simulation before and after assimilation~~MODIS and simulated CER (a and b, in μm), N_d (c and d, in cm⁻³), CLWP (e and f, in g·m⁻²), COT (g and h, dimensionless), CTH (i and j, in m), CTP (k and l, in hPa) and CTT (m and n, in °C) distribution~~s (The r and RMSE in the upper right corner and the subscripts "_bf" and "_af" in the subfigure captions have the same meaning as in the previous figure~~r and RMSE on top right represent the spatial correlation~~

coefficient and root mean square error of the simulated and MODIS data, where RMSE is in the same unit as the variable in the figure)

Based on the model samples matched with the spatio-temporal coordinates of MODIS valid values, wethis study further evaluates the ability of the model to reproduce the satellite-retrieved CLWP-N_d relationship (Figure 6). Due to simulation errors, the scarcity of MODIS samples during the simulation period, satellite retrieval errors, and limitations of the empirical formulas used to calculate N_d, It is found that the simulation with assimilation generally reproduces the increase-decrease-increase variation in CLWP with N_d although the model underestimates CLWP at low N_d as shown by MODIS. The correlation between the simulation and the MODIS CLWP passes the test at the 99% significance level (p<0.01). In contrast, the simulation before assimilation fails to reproduce the above mentioned the MODIS CLWP-N_d relationship. With assimilation, although the model underestimates the CLWP values at low N_d shown by MODI
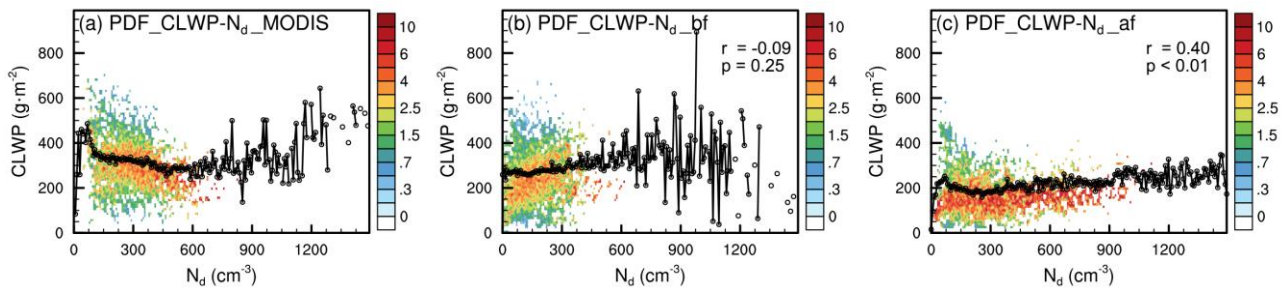
Figure 6. CLWP-N_d relationship of MODIS (a) and simulated before (b) and after (c) assimilation (all samples are assigned into 200 × 100 bins, with each N_d value corresponding to 100 CLWP bins, and the colored dots in the figure represent the number of samples in that CLWP bin as a percentage of all the samples corresponding to that N_d value, i.e., each N_d value corresponds to a total of 100% of the colored dot values. The black line in the figure represents the average of all samples corresponding to each N_d value)

Overall, despite some overestimates and underestimates, the simulations with assimilation generally reproduce the observed values, spatial distributions, temporal variations, and the CLWP-N_d relationship, the model reasonably reproduces the observed meteorological, aerosol and cloud information, providing a basis of confidence for aerosol cloud interaction analysis based on the simulation results.

3.2 Aerosol and cloud droplet distribution in EC and ECO

The aerosol physical and chemical processes, aerosol-cloud interactions, and consequent aerosol and cloud droplet distribution characteristics in EC and ECO (Fig. 67) exhibit distinct discrepancies due to the differences in aerosol properties, topography, and meteorological fields. EC aerosols are mainly primary and secondary aerosols produced by anthropogenic emissions (Fig. 78a a-d and i-l), with small initial particle size. Under the influence of strong surface effects (surface longwave radiation

cooling and terrain uplift) and intense updrafts~~conditions of multiple atmospheric supersaturation pathways~~, these small particles can be activated into cloud droplets, but the limited water vapor hinder further growth of cloud droplets. ECO aerosols are mainly transported from EC (as shown in Fig. 8b, ECO's locally emitted chloride and sodium aerosols contribute less than 20% of the total aerosol mass~~Fig. 7 e g and n p~~), ~~implying~~ so that most aerosols in ECO are anthropogenic aerosols with mostly easily transportable small~~small~~ particles, while with relatively more large particles compared to EC due to sea salt contribution~~compared to EC~~. ~~Meanwhile, compared to EC, there exist a higher proportion of large particles in ECO due to sea salt emissions (Fig. 7 h and m).~~ In addition, the abundant water vapor in ECO provides favorable conditions for aerosol activation and cloud droplet growth, with much more cloud droplets above ~~12.7~~8 μm radius than that in EC though the total cloud droplet number is ~~much~~ lower than that in EC.
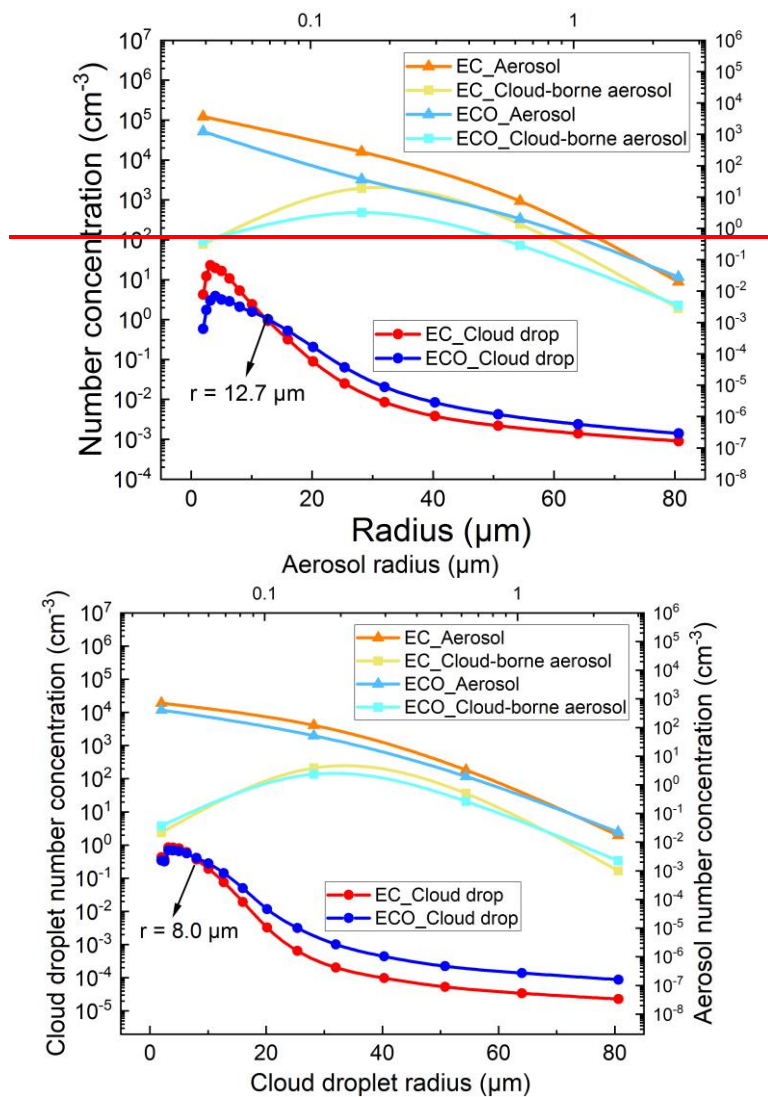
Figure 6~~7~~. Size distributions of cloud droplets, total aerosols and activated (cloud-borne) aerosols in liquid-phase clouds of EC and ECO (in order to obtain the spectral distributions, the aerosols and cloud droplets number concentrations of each bins were first vertically weighted averaged into three-dimensional data containing only time, longitude, and latitude, and only the vertical layers of the liquid-phase cloud were weighted averaged, i.e., the layers with CIWC>0 were excluded from the calculations. Subsequent direct averaging of the three-dimensional number concentrations in each bins obtained the values in figure) ~~in EC and ECO (bottom and left axes correspond to cloud droplets, right and upper axes correspond to aerosols)~~
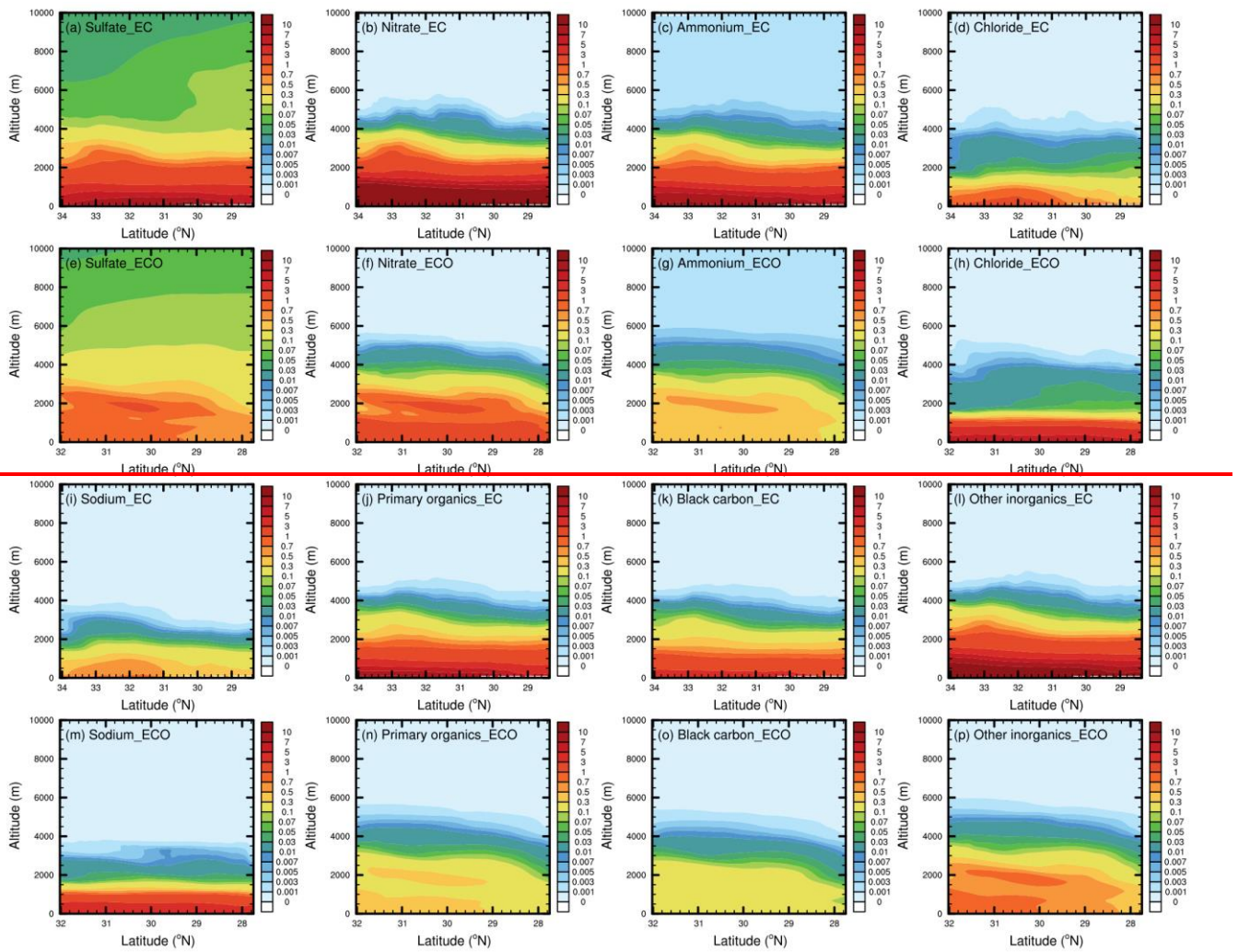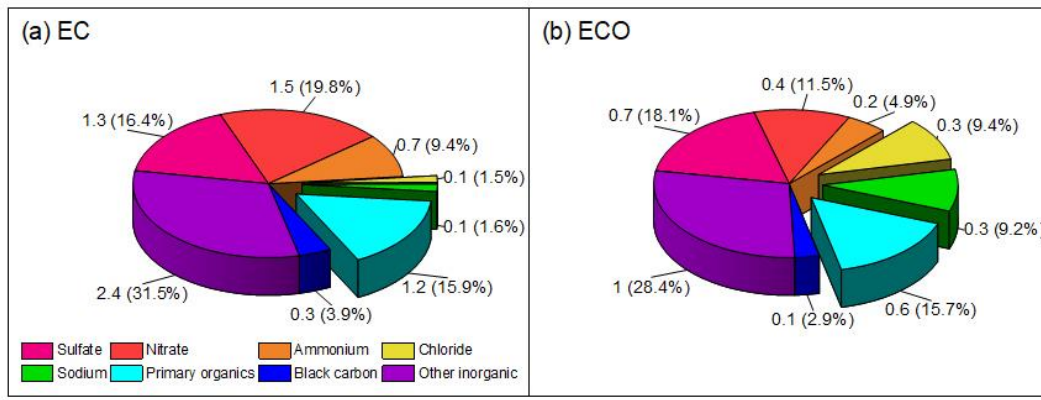
Figure ~~7~~8. Average concentration (in μg·m^{-3}) and percentage of each type of aerosol in EC and ECO during the simulation period (the concentration is a vertically weighted average of each type of aerosol)

~~EC (a-d and i-l) and ECO (e-h and m-p) sulfate, nitrate, ammonium, chloride, sodium, OC, BC and other inorganic (dust) aerosols (in μg·m^{-3}) distributions~~

~~Fig. 9 presents the latitude-averaged variables (N$_{aero}$, N$_d$, CER, supersaturation, water vapour, and wind speed) vary with the height. For N$_d$, supersaturation, and CER, we first filtered out the grid points with CIWC higher than 0 (ice clouds). The lower limit of supersaturation for our statistical analysis is 0, i.e., when the atmosphere is not saturated~~EC and ECO also exhibit clear differences in the spatial distribution of aerosols and cloud droplets. EC aerosol mainly originates from surface emissions, so its ~~aerosol~~ number concentration (N$_{aero}$) gradually decreases from surface to upper layer (Fig. ~~8a~~9a), while ECO aerosols are mainly transported from EC, so N$_{aero}$ hotspot in ECO is located at the transport altitude near 1800 m above sea level (Fig. ~~8b~~9b). In addition to aerosol number and size, atmospheric supersaturation is a determinant of aerosol activation. ~~EC and ECO show clear differences in the atmospheric supersaturation pathway.~~ In EC, the main contributing factors ~~pathways of~~to supersaturation include (1) atmospheric convection, which acts mainly in the areas with relatively strong updrafts and high water vapor content below 4000m altitude. Above 4000 m, the lack of water vapor makes it difficult to supersaturate even with strong updrafts (Fig. ~~8e~~9e, i and k). (2) Water vapor and temperature changes caused by advection, which mainly work~~s~~ in the region of high water vapor content at tens of meters to 1000 m above surface. (3) Long-wave radiative cooling at surface, which acts mainly at night or early morning (Fig. S1), leads to a high supersaturation of the atmosphere (the disappearance of this effect during the daytime makes the temporal average supersaturation near surface relatively low). The high aerosol concentration and supersaturation makes the high N$_d$ near surface (Fig. ~~8e~~9c). (4) Topographic uplift, the forced uplift of topography makes the atmosphere more susceptible to becoming supersaturated~~reach supersaturation~~. In ECO, ~~The main supersaturation pathways in ECO are~~ convection and advection are main influncing factors for supersaturation. Due to the abundant water vapor content, even though ~~the ECO~~ vertical convection is weak, the relatively strong updraft area near 28°N at 2000-4000 m elevation generates much higher supersaturation than the EC (Fig~~s~~. ~~8e~~9e-f and i-l)~~, however, no N$_d$ hotspot is found in this area due to low aerosol concentration (Fig. 8b and d). In winter, at least during this study period, the effect of~~

410

Figure 8~~9~~. EC and ECO aerosol number concentration (in cm⁻³, a-b), N_d in liquid-phase cloud (in cm⁻³, c-d), atmospheric supersaturation (in %, e-f), CER (in μm, g-h), water vapor content (in g·m⁻³, i-j) and vertical wind speed (in m·s⁻¹, k-l) distributions (this figure presents the latitude-averaged variables vary with the height. For N_d, supersaturation, and CER, we first filtered out the grid points with CIWC higher than 0. The lower limit of supersaturation value used in this study is 0. Even if the atmosphere is not saturated, the supersaturation value is 0 rather than a negative value. The average supersaturation characterizes the overall intensity of supersaturation in EC and ECO during the simulation period)

3.3 Aerosol activation of liquid-phase clouds in EC and ECO

To explore the responses of ~~EC and ECO~~ clouds to aerosols and their influencing factors, we perform a statistical analysis on aerosols, clouds and meteorological elements for the grid points with liquid-phase cloud (i.e. $N_d > 1$ cm⁻³, CIWC = 0 and supersaturation > 0) at each time. The statistics are based on each vertical layer and the column (vertical integration of layers with liquid-phase clouds), respectively, with the former providing abundant samples and more immediate and detailed aerosol-cloud relationships~~that are more favorable to avoid fluctuations from individual extreme processes and to obtain the average state of the liquid phase clouds~~, and the latter facilitating relevant studies to compare it directly with information such as satellite retrievals.~~direct comparisons with information such as satellite retrievals.~~

Aerosol activation is the first step of aerosol-cloud interaction, and we ~~analyze~~analyzese the variation of N_d with aerosol (Fig. 10) based on the statistics for each vertical layer ~~(the first two lines of Fig. 9)~~ and for the column ~~(the third line of Fig. 9)~~, respectively. At low N_{aero}, aerosols promote cloud droplet increase by acting as CCN (Figs. 10a-b). As aerosols and cloud droplets increase, more small aerosols (Figs. 10e-f) heighten~~s~~ the requirement of atmospheric supersaturation for aerosol activation, and the consumption of water vapor from cloud droplet growth makes it more difficult for the atmosphere to reach supersaturation, thus suppressing aerosol activation. As shown in Fig. ~~8a~~10a~~and e~~-b, N_d in both EC and ECO exhibit the general trend of increasing first and then decreasing with increasing N_{aero}, but there are some differences between EC and ECO. In EC (Fig. 10~~8~~a-d), strong surface effects and updrafts~~multiple atmospheric supersaturation pathways~~ as well as ~~and~~ abundant aerosols allow N_d to maintain a more persistent ~~increasing~~ trend ~~with N_{aero} until average N_d reaches 6000 cm^{-3}~~. In addition, aerosol activation is not ~~completely~~ suppressed in the near-surface areas with high aerosol concentration~~s (N_{aero} above 40,000 cm^{-3})~~, and aerosols can still be activated at~~-~~ high supersaturation (Fig. 10i) caused by the effects of longwave radiative cooling (the diurnal variation of this effect is also one of the main reasons for the fluctuation of N_d with N_{aero})~~and~~. terrain uplift (the high topographic gradient areas where this action takes effect are also usually~~typically~~ characterized by ~~high concentrations of~~ aerosol accumulation), ~~etc~~and relatively high water vapor content (Fig. 10m) near surface. In ECO ~~(Fig. 9e h)~~, the absence of surface effects as in EC and weaker updrafts limit its supersaturated water supply~~the dominance of water vapor variation on aerosol activation is more pronounced~~, and the supersaturation (Fig. 10f) shows a more pronounced and synchronized variation with variation in ambient water vapor content (Fig. 10n) and decreases rapidly with increasing N_{aero} after N_d peak~~shows a steady decreasing trend with increasing N_{aero}. Once~~After N_d reaches its peak~~N_{aero} exceeds 10000 cm^{-3} (average N_d reaches 3000 cm^{-3})~~, the increase in small aerosols and the decrease in supersaturation prevent ~~its~~ N_d from continuing to increase and N_d starts to show a decreasing trend~~.~~, without fluctuations like EC. Unlike the statistics for each vertical layer, the statistics for the column show that N_d exhibits an increase with AOD followed by a general maintenance (Figs. 10c-d). In EC, the maintenance is mainly due to a higher percentage of easily activated large particles at high AOD (Fig. 10g), while in ECO it is mainly due to an overall higher supersaturation (Fig. 10l) associated with the abundant water vapor (because column sampling cannot accurately match aerosol-cloud related variables in vertical coordinates based on the intensity of cloud processes, column sampling exhibits a less immediate and precise relationship between supersaturation and water vapor content than sampling of each vertical layer. So in terms of column statistics, although ECO water content is close to EC, its average supersaturation is much higher than that of EC).~~The statistics on the column (Fig. 9i l) also show that the variation of N_d with AOD in EC is much flatter, while N_d decreases rapidly after AOD exceeds 0.8 in ECO. It is worth mentioning that the high AOD value in EC is dominated by large particles, which is one of the reasons why the trend of EC N_d decreasing with AOD is flatter, whereas the high AOD value in ECO depends largely on the transport of EC aerosols, and the small particles that are more easily transported make its high AOD value mostly attributed to a large amount of small particles, which exacerbates the decrease ECO N_d with AOD.~~
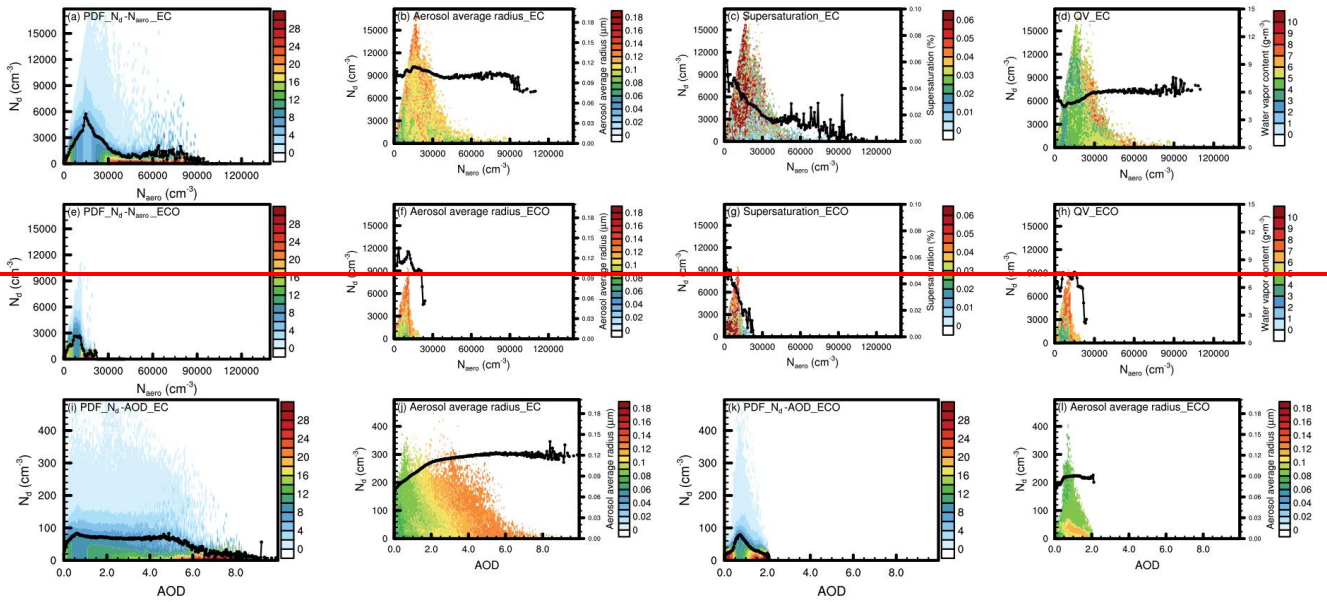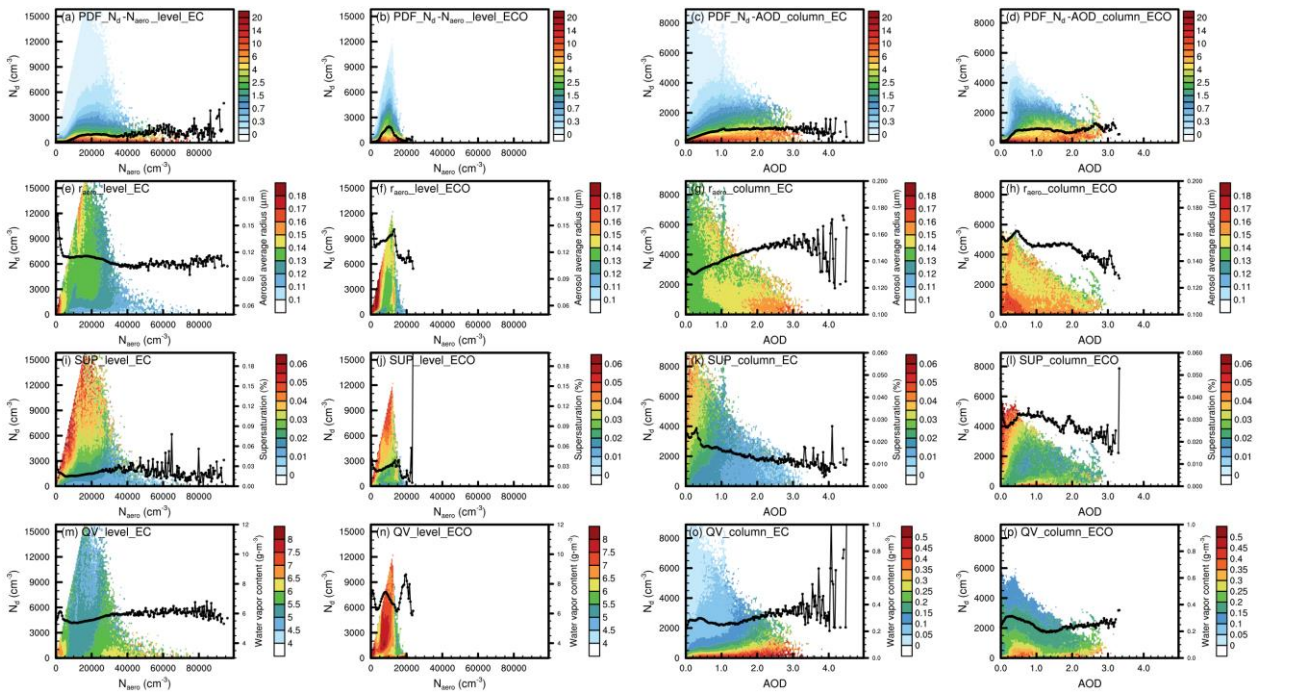
Figure 910. N_d varies with aerosol (a-d, the unit for colored dots is %, while the unit for the black lines is the left vertical axis unit), as well as the aerosol volume average radius (e-h, the colored dots and black lines of these figures and all subsequent figures correspond to the units on the right vertical axis unit), supersaturation (i-l) and water vapor content (m-p) varies with N_d and aerosol in EC and ECO based on statistics at each vertical layer (two columns on the left) and column (two columns

on the right), respectively (samples were taken from each time and each grid point, and each sample contained N_{aero} or AOD, N_d, aerosol volume mean radius, supersaturation, and water vapor content values. These samples were placed into 200 aerosol $\times$ 100 N_d bins according to the interval in which their N_{aero} or AOD values and N_d values were located. The colored dots in Figs. a-d represent the proportion of that bin's sample number to the total number of samples of the 100 bins corresponding to the N_{aero} or AOD interval, i.e., the total value of all colored dots corresponding to each N_{aero} or AOD interval is 100%. The black lines in Figs. a-d represent the average N_d of all samples at the corresponding N_{aero} or AOD intervals. The colored dots in Figs. e-p represent the average values of the variable for all samples in the bin corresponding to the aerosol and N_d intervals. The black lines in Figs. e-p represent the average value of this variable in all samples corresponding to this aerosol interval)~~Probability density distribution functions (sum of probabilities corresponding to 1 for each N_{aero} or AOD value) and means (lines in a, e, i and k) of the simulated N_d relative to N_{aero} (a and e) and AOD (i and k), as well as the values (corresponding to the left and bottom axis) of aerosol average radius (b, f, j and l), supersaturation (c and g) and water vapour content (d and h) along with their mean changes (lines in figures, corresponding to the right and bottom axis) relative to N_{aero} (the first two lines) and AOD (the third line) in EC (a-d and i-j) and ECO (e-h and k-l). The first two lines are based on statistics for each vertical layer, and the third line is based on statistics for column~~

To investigate the influence of meteorological conditions on aerosol activation, a statistically analysis on the variation of N_d ~~and~~ to N_{aero} ratio (characterizing the intensity of aerosol activation) with N_{aero} for different zonal wind speed (U), meridional wind speed (V), vertical wind speed (W), temperature, water vapor content, as well as temperature and water vapor changes at that time compared to the last time (~~since~~ the model outputs once per hour, the changes are the values of the current time ~~value of the sample~~ minus the previous hour's value) are presented in Fig. ~~10~~11. In EC, ~~when both zonal and meridional wind speeds are close to 0 m·s⁻¹, a large number of aerosols accumulate and strong aerosol activation can occur under the effect of radiative cooling at surface. Exceptionally, strong aerosol activation~~high N_d to N_{aero} ratio ~~also~~ occurs when the zonal wind speed < -6 m·s⁻¹ or meridional wind speed < ~~-8~~-7 m·s⁻¹, the former due to large amounts of water vapor from the ocean brought by easterly winds (Fig. S2b) and the latter due to cold air brought by northerly winds (Fig. S2a) and uplift caused by the south high and north low topography in EC (Fig. 1). The overall high N_d to N_{aero} ratio~~strong aerosol activation~~ is exhibited at relatively high~~er~~ vertical wind speeds, but aerosol activation is also found when the vertical airflow is weak or dominated by downdraft due to the influence of advection at tens of meters to 1000 m above surface, topographic uplift, and long-wave radiative cooling at surface~~. Aerosol activation is hardly occur in the high altitude downdraft dominated areas where N_{aero} < 10000 cm⁻³ and W < 0 m·s⁻¹. Liquid phase clouds of EC appear mainly under the conditions of -5-14 °C temperature and 3-13 g·m⁻³ water vapor content. Ice phase processes occur frequently below -5 °C, and in addition the atmosphere is difficult to reach supersaturation in areas with water vapor content below 3 g·m⁻³ or water vapor content above 13 g·m⁻³ and temperature above 14 °C (temperature and water vapor content show generally consistent spatial distribution)~~. High N_d to N_{aero} ratio in EC mainly occurs at low temperatures and low humidity conditions, which is due to the fact that the temperature and humidity horizontal gradients are essentially the same (Fig. S2), and EC with low overall water vapor content is more likely to reach

500 supersaturation at both low temperature and water vapour content, and becomes increasingly difficult to reach supersaturation when the temperature and humidity are simultaneously increased. -The increase in water vapor and decrease in temperature contribute to EC aerosol activation, but the strong surface effects and updraftsdiversity of atmospheric supersaturation pathways enables aerosol activation to occur even at significant warming or humidity reductionreduced water vapor or elevated temperatures.
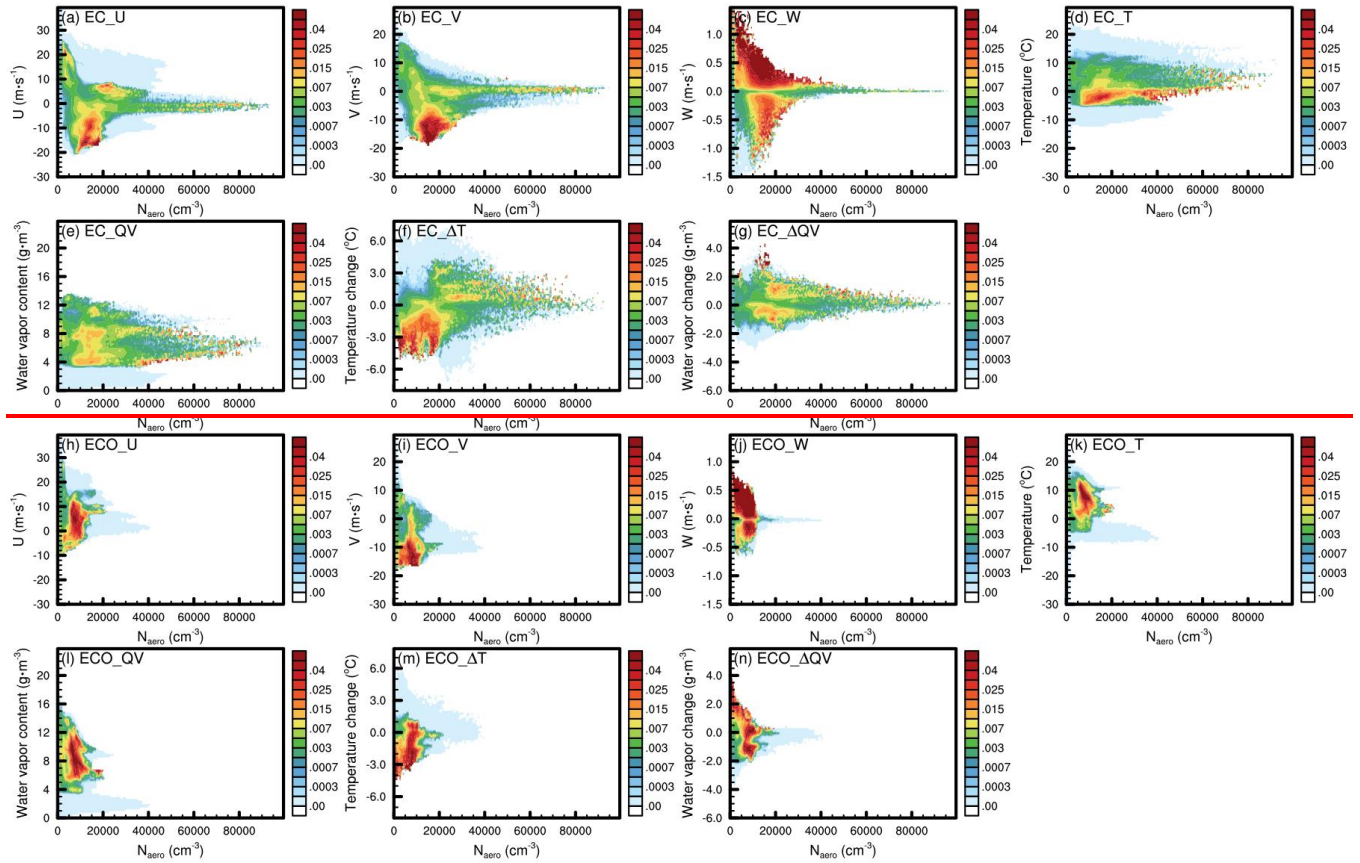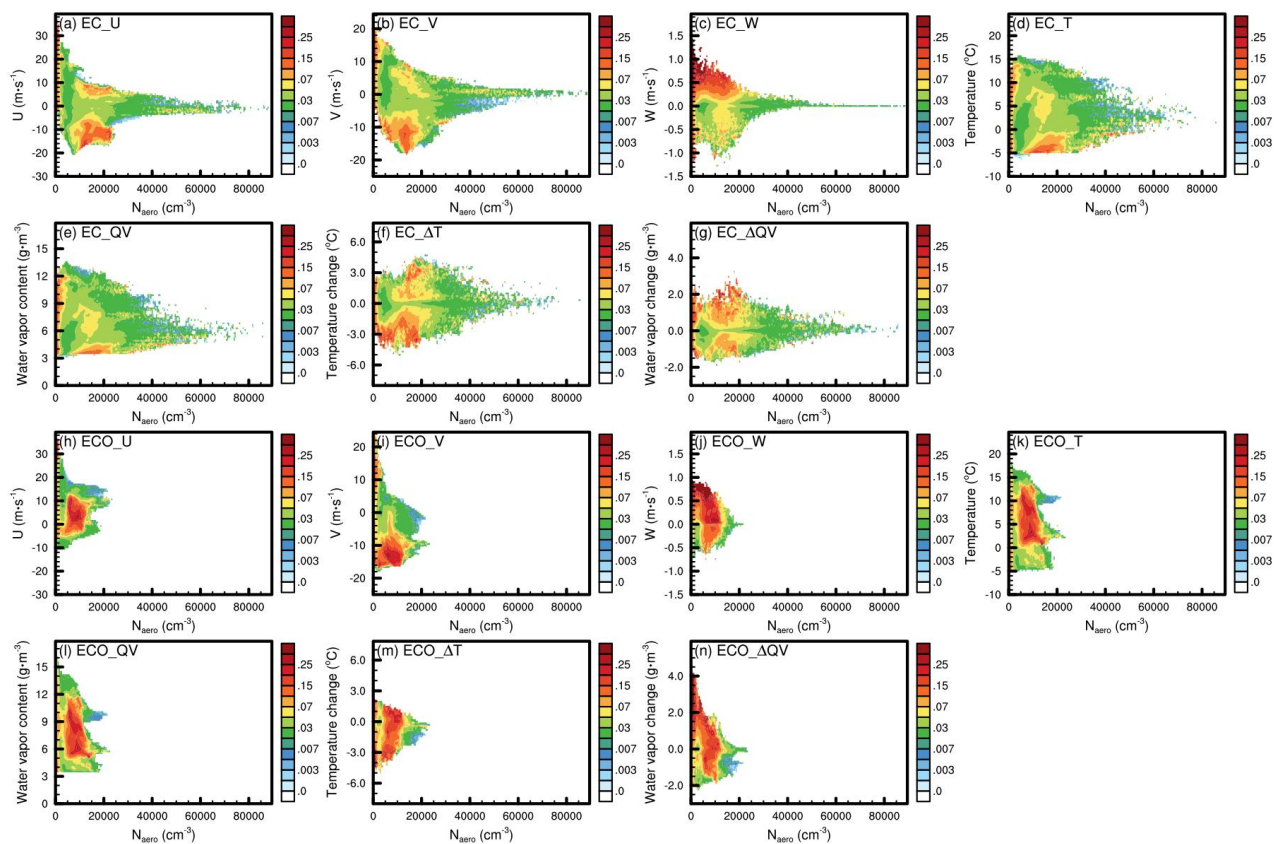
Figure ~~10~~11. Variation of EC (a-g) and ECO (h-n) N_d to N_{aero} ratio (unit: $cm^{-3} \cdot cm^3$) with N_{aero} at different U-wind (a and h), V-wind (b and i), W-wind (c and j), temperature (d and k), water vapor content (e and l), temperature change~~variation~~ (f and m) and water vapor change~~variation~~ (g and n, this figure is sampled at each vertical layer and calculated in the same way as Fig. 10, except that the bin of N_d is replaced by the bin of each meteorological element)

In ECO, the zonal wind speed favourable to aerosol activation is below 0 m·s⁻¹ or 0-~~12~~13 m·s⁻¹, with the former ensuring the supply of water vapor and the latter providing more abundant aerosols, while at zonal wind speed above ~~12~~13 m·s⁻¹, the excessively dry air from land makes the atmosphere difficult to reach supersaturation, despite the large amount of aerosols brought by the westerly wind. The meridional wind speed suitable for ECO activation is mainly below -8 m·s⁻¹, the cold air brought by strong northerly winds makes it easier for the atmosphere to reach supersaturation. The abundance of water vapor makes ECO more susceptible to reach supersaturation by updrafts, making its activation exhibit a high sensitivity to vertical wind speeds. Compared to EC, ECO's more abundant water vapor content ~~allows it to~~ generate higher N_d to N_{aero} ratio at higher temperatures and humidity conditions. In addition, ECO aerosol activation is more limited by cooling and humidification due to atmospheric motion (no strong surface effects like in EC), its high N_d to N_{aero} ratio is clearly skewed toward high humidification and cooling conditions compared to EC.~~The temperature and water vapor conditions suitable for liquid phase~~

clouds in ECO are the same as in EC, with the difference that the abundant water vapor in ECO results in clearly stronger activation at higher temperatures than in EC.

3.4 Impact of aerosols on development of liquid-phase clouds

Aerosol activation alters cloud droplet size distribution and consequent changes in cloud microphysical and dynamical
525 processes, which is also known as rapid adjustment (Heyn et al., 2017; Mulmenstadt and Feingold, 2018). We discuss the variations of CLWC and CER with increasing N_d (Fig.12) for precipitation clouds (rainwater content above 1 mg·m^{-3} for each vertical layer and above 1 g·m^{-2} for column~~raindrop number concentration above 0 m^{-3}~~) and ~~non-precipitation~~non-precipitating clouds (rainwater content below 0.001 mg·m^{-3} for each vertical layer and below 0.001 g·m^{-2} for column~~raindrop number concentration of 0 m^{-3}~~). For precipitation clouds, CLWC in both EC and ECO ~~precipitation clouds~~ show a trend of rapid
530 increase followed by a gradual slowdown (the net influence of water content limitation, evaporation and precipitation effects, accompanied by the decrease in CER) with N_d. The difference lies in that the abundant water vapor in ECO makes its CLWC increase much faster than that in EC when N_d is very low, whereas the higher aerosol concentration, strong surface effects and updrafts in EC enable it to have a wider N_d range and can produce higher CLWC. For~~In relatively dry~~ non-precipitating clouds, the consumption of limited supersaturated water by aerosol activation and cloud droplet growth causes clear decreasing trends
535 of CLWC with N_d after CLWC increasing to a certain level. The difference between the two regions is that more limited supersaturated water supply in ECO causes its CER to decrease faster and CLWC to start decreasing earlier.

~~In EC, the multiple atmospheric supersaturation pathways and abundant aerosols cause wide N_d range (Fig. 11a-d). Higher N_d allows the precipitation cloud to reach a higher CLWC in EC than that in ECO, but the influence of precipitation and evaporation gradually slows down the increase of CLWC with N_d. When N_d exceeds 16000 cm^{-3}, CLWC decreases rapidly as~~
540 ~~a result of the precipitation and higher evaporation triggered by the small cloud droplets. Compared to precipitation clouds, non-precipitation clouds in EC have lower CLWC, but the absence of precipitation process and weaker evaporation due to the lower difference in intracloud and ambient water vapor pressure result in a more steady increase in their CLWC with N_d, and after N_d exceeds 12000 cm^{-3}, the decreasing tendency of CLWC is less pronounced. In ECO (Fig. 11e-h), although the supersaturation pathway limits the increase of N_d and CLWC, abundant water vapor causes its CLWC to increase faster at low~~
545 ~~N_d as well as a weaker decrease in CLWC at high N_d. In addition, the scarcity of non-precipitating cloud samples under abundant water vapor results in a stronger volatility in CLWC.~~
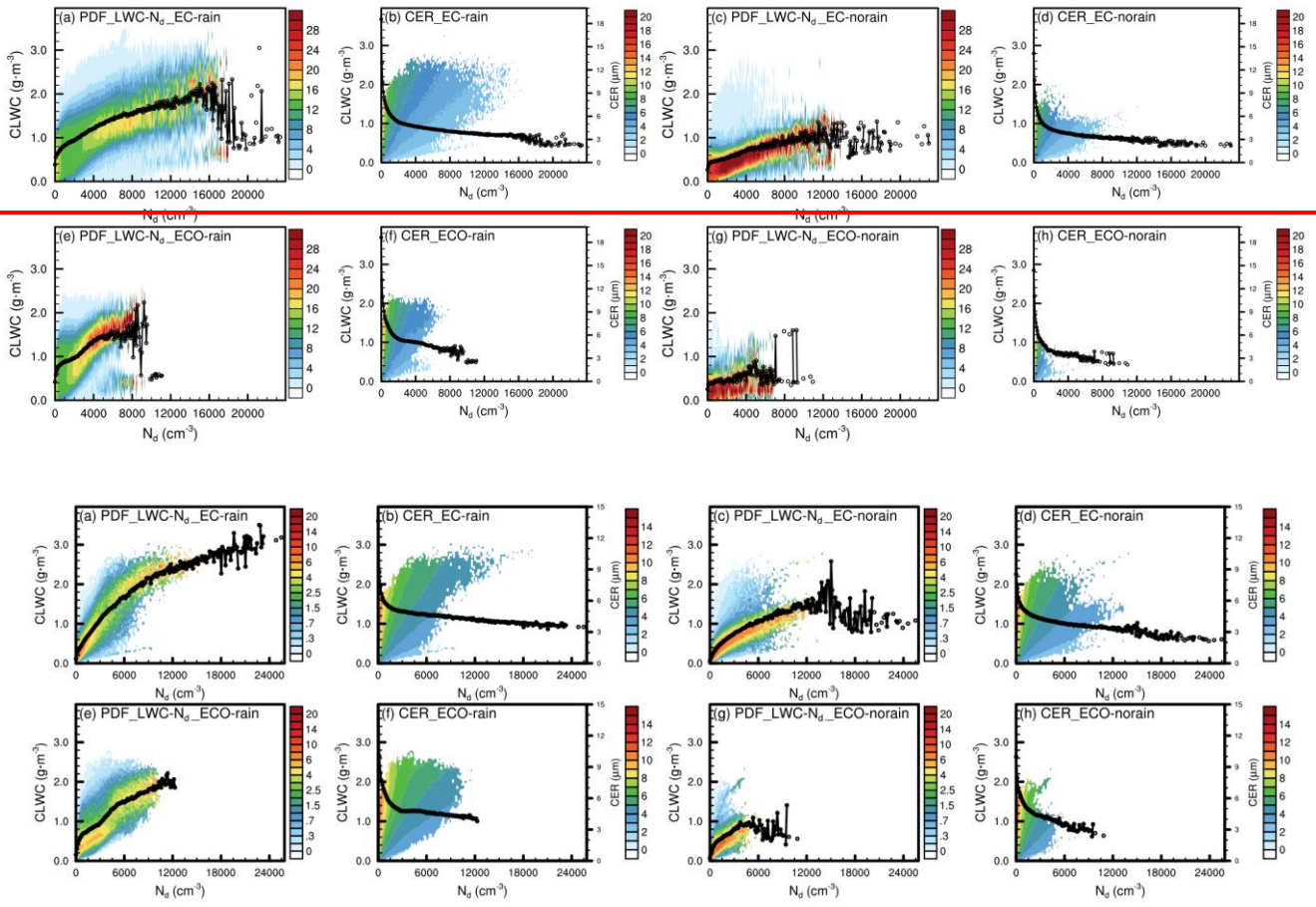
Figure 1112. CLWC varies with N_d (a, c, e and g), and CER varies with CLWC and N_d (b, d, f and h) for precipitating (two columns on the left) and non-precipitating (two columns on the right) clouds in EC (a-d) and ECO (e-h), based on statistics at each vertical layer (interpretation of the figure is the same as in the caption of Fig. 10)~~Probability density distribution functions (sum of probabilities corresponding to 1 for each N_d value) and means (lines in the figures) of CLWC relative to N_d (a, c, e, and g), as well as the CER values (b, d, f, and h, corresponding to the left and bottom axis) and their mean changes relative to N_d (lines in the figures, corresponding to the right and bottom axis) of precipitation clouds (a-b and e-f) and non-precipitation clouds (c-d and g-h) in EC (a-d) and ECO (e-h)~~

We further ~~analyse~~examine the variations of CLWP and its related elements with AOD based on the statistics of the column (Fig. 13)~~, in order to provide direct comparisons with satellite retrievals.~~. For ~~In~~the precipitation clouds~~, of EC and ECO~~, with the increase of AOD, CLWP remains generally stable (the combined effects of cloud droplets and precipitation changes), while N_d increases initially and then decreases (the decrease in N_d of ECO at AOD 1.5-2.0 is due to a decrease in water vapor content caused by individual processes as shown in Fig. 10p, and simulations and statistical analyses for longer

time periods can attenuate the effect of such individual processes), and both CER and rain water path (RWP, i.e. rainwater column content) decrease. ~~with increasing AOD~~There is a bi-directional interaction between RWP and aerosols, i.e., low AOD is largely resulted from the washout of aerosols by precipitation, whereas increasing N_d and decreasing CER due to increasing aerosols also decrease the RWP. For non-precipitation clouds~~With almost no influence of precipitation~~, CLWP increases with AOD, while N_d firstly increases and then shows a weak decreasing trend~~remains unchangedmaintains with AOD in non-precipitating clouds.~~~~In EC, heavy precipitation (Fig. 12d) causes a rapid decrease in CLWP at low AOD (Fig. 12a). Once AOD exceeds 2, small CER inhibits precipitation and the decrease in CLWP, sufficient aerosols and multiple atmospheric supersaturation pathways lead to the stabilization of CLWP. With increasing AOD, CER and N_d in EC exhibit decreasing followed by increasing and increasing followed by decreasing trends, respectively, with both exhibiting significant fluctuations at high AOD values (since Fig. 12c samples N_d based on different intervals of ADO and CLWP, its variation of N_d with AOD is close but not identical to Fig. 9i). When AOD is lower than 4, the variation of rain water path (RWP, i.e., column rain water content) is dominated by the variation of N_d, i.e., the increase of N_d leads to the decrease of CER and RWP. The dominance of large aerosol particles at high AOD (fig 9j) gradually increases the RWP after AOD exceeds 4, but as precipitation consumes the CLWP, the RWP gradually decreases after AOD exceeds 8. Compared to EC, ECO, where the supersaturation pathway is more monotonous, is also more monotonous in the variation of cloud parameters, i.e., both CLWP and RWP show a steady decreasing trend with increasing AOD. Due to the characteristics of the model calculation and the limitation of the column statistics, the obtained samples of non-precipitation clouds (RWP = 0 g·m⁻²) are rare, and the CLWP of all clouds (precipitation and non-precipitation clouds, Fig. 12l and p) shows almost the same trend as that of precipitation clouds. In these samples, EC non-precipitation clouds exhibit cloud parameter variations that are generally similar to precipitation clouds but more moderate, mainly due to weaker in-cloud processes. ECO, due to a limited number of samples, displays more pronounced variations in cloud parameters for non-precipitation clouds compared to precipitation clouds.~~
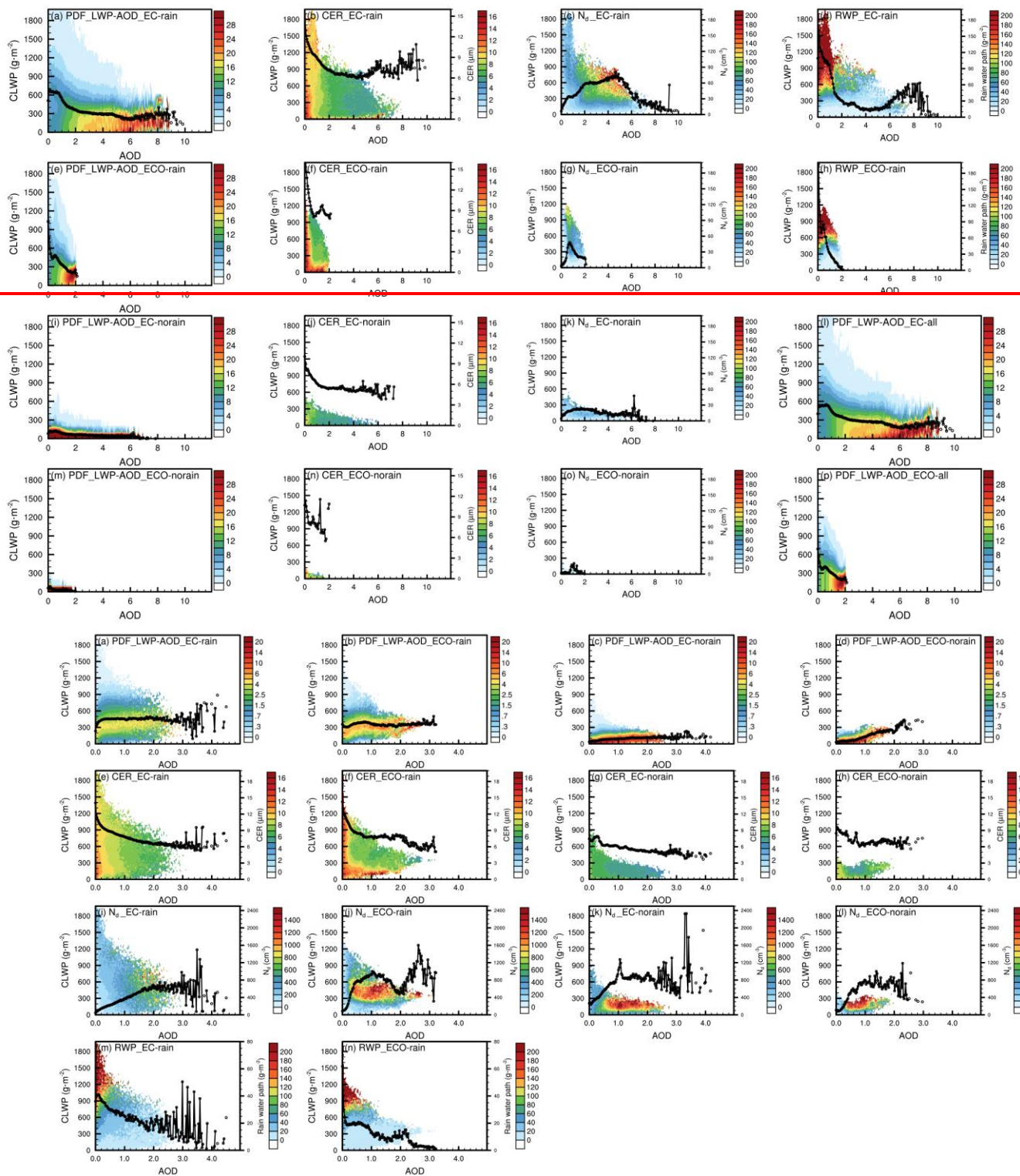
Figure 1213. CLWP varies with AOD (a-d), as well as CER (e-h), N_d (i-l) and RWP (m-n) varies with CLWP and AOD for precipitation clouds (two columns on the left) and non-precipitating clouds (two columns on the right) in EC and ECO (interpretation of the figure is the same as in the caption of Fig. 10)

~~Probability density distribution functions (sum of probabilities corresponding to 1 for each AOD value) and means (lines in the figures) of CLWP relative to AOD (a, e, i, l, m and p), as well as the variation of CER (b, f, j and n), N_d (c, g, k and o) and column rain water path (RWP, d and h) with AOD of precipitation clouds (a-h), non-precipitation clouds (i-k and m-o) and all clouds (l and p) in EC (a-d and i-l) and ECO (e-h and m-p)~~

Fig. ~~13~~ 14 exhibits the effects of different meteorological and aerosol conditions on CLWC. The CLWC and N_{aero} ratio (characterizing the speed of cloud development) under different meteorological and N_{aero} conditions shows generally similar variation to the N_d and N_{aero} ratio in Fig. 1~~1~~0, with only some minor differences. Compared to the high N_d and N_{aero}~~activation~~ ratios exhibited in Fig. 10, which tend to occur at medium N_{aero}, the high CLWC and N_{aero} ratios at low N_{aero} are more heavily weighted due to the more abundant water vapor supply and weaker evaporation when there are fewer but larger cloud droplets.
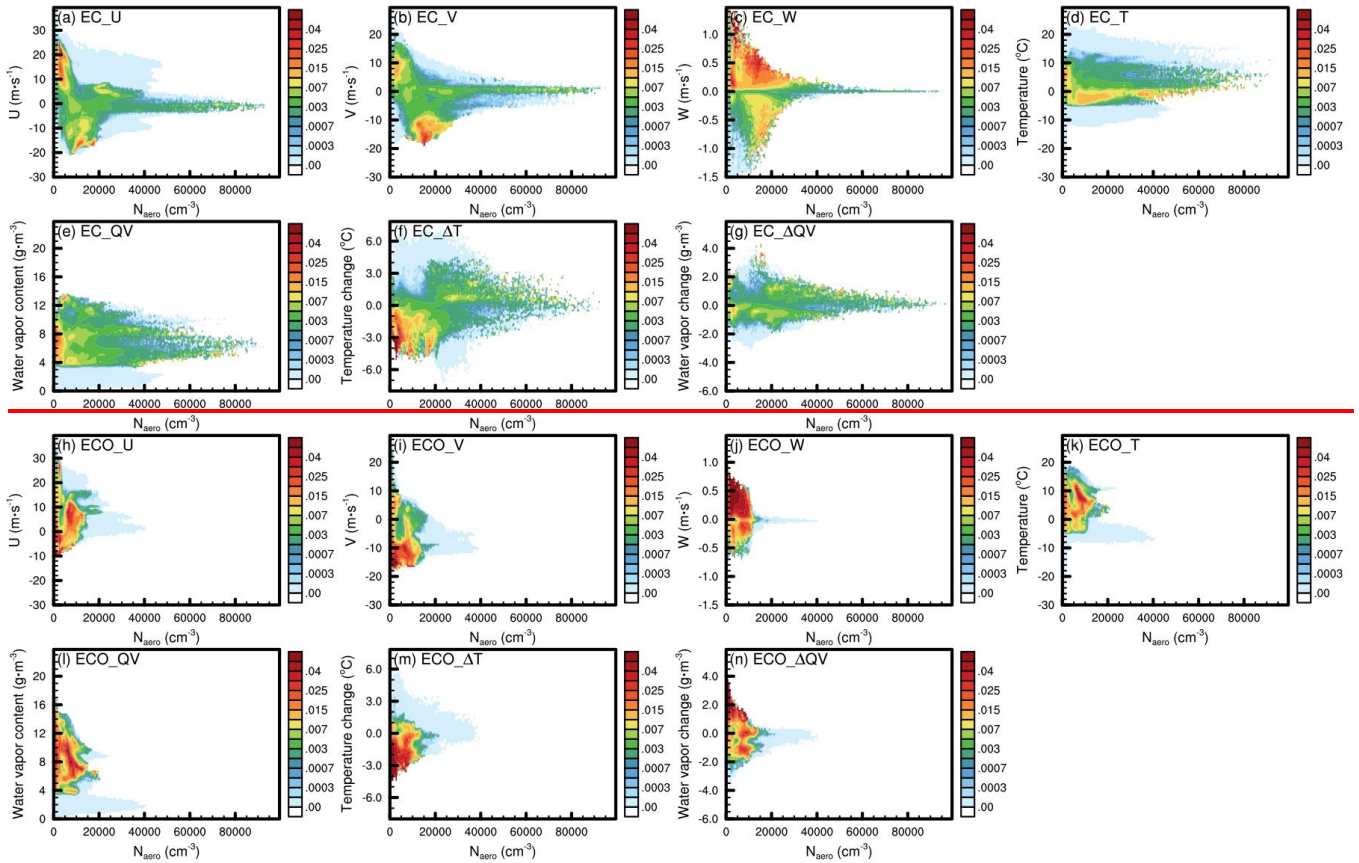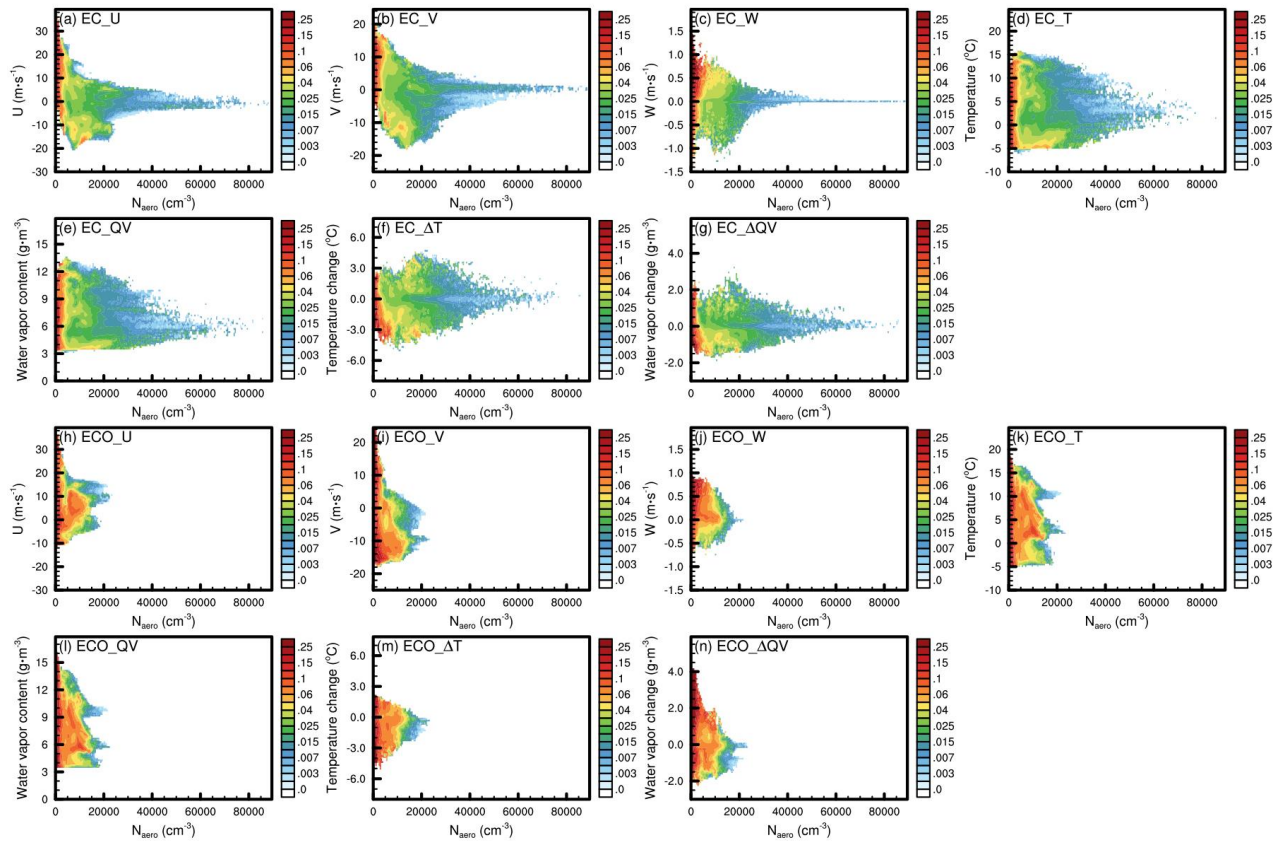
Figure 1~~4~~3. Same as Fig. 11 but for CLWC to N_{aero} ratio (unit: mg·m^{-3}·cm^3) ~~Variation of EC (a-g) and ECO (h-n) CLWC to N~~_{~~aero~~} ~~ratio (unit: mg m~~$^{-3}$~~·cm~~^{3}~~) with N~~_{~~aero~~} ~~at different U-wind (a and h), V-wind (b and i), W-wind (c and j), temperature (d and k), water vapor content (e and l), temperature variation (f and m) and water vapor variation (g and n)~~

4 Summary ~~Conclusion~~

In this study, aerosol-cloud interactions in liquid-phase clouds over eastern China (EC) and its adjacent ocean region (ECO) in winter are explored based on the WRF-Chem-SBM model in which a spectral-bin cloud microphysics (SBM) and online aerosol module (MOSAIC) are coupled.

The impact of four-dimensional data assimilation on the simulation and performance of the coupling system is firstly evaluated using multiple observations. With assimilation, the simulated meteorological field is generally closer to the observations both in values and spatial distribution. ~~Overall we see positive effects on the simulated meteorology by using data assimilation, especially below 800 hPa, which is very beneficial for the simulation of low clouds that dominate in winter.~~ The simulations of precipitation and aerosol are effectively improved by optimizing the meteorological field, the RMSE of simulated precipitation versus observation is reduced by 61.5%, and the temporal correlation of simulated PM$_{2.5}$ with

observations at each site is improved by 9.5% on average. ~~The assimilation, while affecting the meteorological field and aerosol simulations, also improves the model's ability to reproduce satellite-retrieved cloud parameters and CLWP N_d relationship, providing great help in exploring the aerosol-cloud interactions in EC and ECO.~~ and the observed and simulated precipitation ~~and near-surface $PM_{2.5}$ RMSEs are reduced by 60.4% and 21.3%, respectively. By using four-dimensional assimilation, the WRF-Chem-SBM model reasonably reproduces satellite-retrieved cloud parameters, and providing a confidence basis for the analysis of aerosol-cloud interactions in this study.~~

~~Differences in meteorological, topographic, and aerosol conditions make EC and ECO aerosol activation distinctly different. There are four main atmospheric supersaturation pathways in EC, namely updrafts mainly acting below 4000m altitude, advection mainly operating at tens to 1000 m, long-wave radiative cooling near surface at night to early morning, and topographic uplift in areas of large topographic gradient. The multiple supersaturation pathways produce a large number of cloud droplets in EC, but the limited water vapor over land constrains the growth of cloud droplets, causing them to exhibit a large total quantity but generally small size. In contrast, only convection and advection act as the two main supersaturation pathways in ECO. The abundant water vapor contributes to the overall higher supersaturation and more suitable growth environment for activated cloud droplets in ECO, where the number of cloud droplets above 8 μm radius is much higher than that in EC, although the total N_d is lower than that in EC.~~

~~The abundant water vapor in ECO produce higher supersaturation than EC with weaker updraft near 28°N at 2000-4000 m elevation where convection dominates atmospheric supersaturation, but no N_d hotspot appears in this area due to the limitation of N_{aero}. The area around 1000 m, where both water vapor and aerosols are relatively abundant, is the N_d hotspot in ECO, and the abundant water vapor provides powerful support for the cloud droplet growth, so that the ECO cloud droplets over 12.7 μm radius are much more than those in EC with much fewer total quantity than EC.~~

We explore the responses of clouds to aerosols and their influencing factors ~~the effects of different meteorological and aerosol conditions on cloud formation and development~~ through the statistics of liquid-phase cloud samples. Statistics on each vertical layer show that in both EC and ECO, N_d exhibits an overall increasing and then decreasing trend with N_{aero}. The difference is that the strong surface effects (surface longwave radiation cooling and terrain uplift) in EC ~~allow it to still appear~~ induce high N_d ~~in the~~ near-surface ~~region~~ with high N_{aero}, whereas in ECO, N_d increases faster at low N_{aero} due to abundant water vapor, ~~but also because of the dependence of its activation on supersaturated water vapor, it~~ and decreases rapidly after the peak of N_d. However, the statistics on the entire column show that N_d increases with AOD and then generally remains unchanged ~~maintains~~ (there is no clear decrease as in the statistics on each vertical layer), partly because high AOD does not correspond to high N_{aero}, and also because the statistics on column are not as detailed and immediate as those on each vertical layer. ~~Our analysis of aerosol activation shows that in both EC and ECO, N_d exhibits a trend of increasing and then decreasing with increasing N_{aero}. The difference between EC and ECO is that multiple supersaturation pathways and abundant aerosols in EC cause N_d to exhibit a much robust increasing trend compared to ECO at low N_{aero} and strong fluctuations at high N_{aero}. While in ECO, the strong dependence of aerosol activation on water vapor content makes N_d maintain only an unsteady increasing trend with N_{aero}. Once N_{aero} exceeds 10000 cm^{-3} (average N_d exceeds 3000 cm^{-3}), the consumption of water vapor~~

645 ~~by cloud droplet growth makes it difficult for the atmosphere to reach supersaturation, together with the higher percentage of small aerosols at high N_{aero}, ECO N_d increase is gradually suppressed. In EC, favourable meteorological conditions for aerosol activation include: (1) aerosol accumulation under static or weak wind conditions and high supersaturation due to radiative cooling at surface, (2) moist air brought by strong easterly wind, (3) cooling and topographic uplift due to strong northerly wind, and (4) strong updraft. In ECO, the meteorological conditions suitable for aerosol activation include (1) aerosol-rich and~~

650 ~~not excessive dry airflow from moderate westerly wind, (2) cooling due to strong northerly wind, and (3) updraft. In general, the contribution of cooling to aerosol activation is more pronounced relative to humidification in EC and ECO.~~

~~We further discuss the effect of aerosol-induced N_d variations on CLWC.~~ Statistics on each vertical layer show that in precipitation clouds, CLWC increases with N_d and its increase rate gradually slows down, whereas in non-precipitation clouds

655 with lower water content, CLWC decreases with N_d after its increase to the peak. The difference between EC and ECO precipitation clouds lies in that the abundant aerosol, strong surface effects and updrafts allow EC to produce higher N_d and CLWC, and the more abundant water vapor in ECO enables its CLWC to increase faster at low N_d. The difference between the non-precipitating clouds in the two regions is that the insufficient supply of supersaturated water due to fewer and less intense processes affecting supersaturation in ECO leads to its CER decreasing rapidly, and the CLWC begins to decrease at

660 lower N_d than in EC. We further analyse the variation of CLWP with AOD based on the statistics on column. For precipitation clouds, CLWP remains generally stable with AOD without significant variation due to the combined effect of precipitation and aerosol. While in non-precipitating clouds, which are almost unaffected by precipitation, CLWP increases gradually with AOD.

We explore the effects of different meteorological and aerosol conditions on N_d to N_{aero} ratio (characterizing the intensity

665 of aerosol activation) and CLWC to N_{aero} ratio (characterizing the speed of cloud development). In EC, favourable meteorological conditions for aerosol activation include: (1) moist air brought by strong easterly wind, (2) cooling and topographic uplift due to strong northerly wind, and (3) strong updraft. In ECO, the meteorological conditions suitable for aerosol activation include (1) aerosol-rich and not excessive dry airflow from moderate westerly wind, (2) cooling due to strong northerly wind, and (3) updraft. ECO's abundant water vapor allows it to produce high N_d to N_{aero} ratio at higher

670 temperature environments than EC, but fewer and less intense processes affecting supersaturation make its activation more dependent on strong humidification and cooling (whereas EC's strong surface effects can enable high N_d to N_{aero} ratio to occur even under significant warming or humidity reduction). Meteorological conditions suitable for CLWC increase are close to aerosol activation, while high CLWC to N_{aero} ratios occur more often at low N_{aero} conditions compared to moderate N_{aero} conditions where high N_d to N_{aero} ratio appears. ~~For precipitation clouds, CLWC increases and then decreases with increasing~~

675 ~~N_d in both EC and ECO. The high N_d supported by multiple supersaturation pathways in EC causes higher CLWC than ECO at lower water vapor content, while ECO exhibits a more rapid increase in CLWC before the increase in CLWC stagnates. Due to the weaker intracloud processes, the CLWC variation trend of EC non-precipitation clouds is gentler than that of precipitation clouds. In contrast, ECO shows more pronounced fluctuations in its non-precipitation cloud CLWC variation~~

35

~~than precipitation clouds due to the scarcity of non-precipitation cloud samples under abundant water vapor. We analyze the~~
680 ~~variation of CLWP with AOD based on the statistics on column. In both EC and ECO, the strongest precipitation occurs at~~
~~AOD less than 1, causing CLWP to decrease rapidly with AOD. With increasing AOD, the increase in N_d inhibits the reduction~~
~~of CLWP in both EC and ECO, and this inhibition is more pronounced in EC where atmospheric supersaturation is less~~
~~dependent on water vapor. As AOD increases further and N_d begins to decrease, the lack of water vapor and the decrease in~~
~~aerosol particle size cause CLWP in ECO to decrease rapidly, while the dominance of large particles at high AOD in EC allows~~
685 ~~its CLWP to remain stable. Meteorological and aerosol conditions suitable for EC and ECO cloud development are basically~~
~~the same as those suitable for aerosol activation, with the difference that high aerosol activation ratios occur mainly under~~
~~moderate N_{aero} conditions, whereas high CLWC and N_{aero} ratios often occur under low N_{aero} conditions in addition to moderate~~
~~N_{aero} conditions.~~

690 ~~+++++~~

Data availability. The model outputs are available upon request (the namelist file of the model simulation is attached as Supplement A), the other data can be accessed from the websites listed in Sect. 2.

Author contributions. JZ and XM designed and conducted the model experiments, analysed the result and wrote the paper.
695 XM developed the project idea and supervised the project. XM, JQ and HJ proposed scientific suggestions and revised the paper.

Competing interests. One author (JQ) is a member of the editorial board of journal ACP, and the authors have no other competing interests to declare.

700

Acknowledgements. This study is supported by the National Natural Science Foundation of China (Grants 42061134009 &41975002) and the Postgraduate Research and Practice Innovation Program of Jiangsu Province (Grant KYCX22_1151). The numerical calculations in this paper was conducted in the High-Performance Computing Center of Nanjing University of Information Science & Technology. We express our gratitude to Dr. Jiwen Fan of Argonne National Laboratory for providing
705 the code for the WRF-Chem-SBM model and Prof. Qian Chen of Nanjing University of Information Science & Technology for providing advice on this study. We are grateful to the National Aeronautics and Space Administration, the National Center for Environmental Prediction, MEIC Support Team, the Chinese National Meteorological Center and China National Environmental Monitoring Centre for providing the MODIS and GPM data, FNL and observation subsets, MEIC emission inventory, MICAPS data and $PM_{2.5}$ data respectively.

References

Albrecht, B. A.: Aerosols, cloud microphysics, and fractional cloudiness, Science 245, 1227-1230, https://doi.org/10.1126/science.245.4923.1227, 1989.

Arias, P., Bellouin, N., Coppola, E., Jones, R., Krinner, G., Marotzke, J., Naik, V., Palmer, M., Plattner, G.-K., Rogelj, J., Rojas, M., Sillmann, J., Storelvmo, T., Thorne, P., Trewin, B., Achutarao, K., Adhikary, B., Allan, R., Armour, K., Bala, G., Barimalala, R., Berger, S., Canadell, J. G., Cassou, C., Cherchi, A., Collins, W. D., Collins, W. J., Connors, S., Corti, S., Cruz, F., Dentener, F. J., Dereczynski, C., Di Luca, A., Diongue Niang, A., Doblas-Reyes, P., Dosio, A., Douville, H., Engelbrecht, F., Eyring, V., Fischer, E. M., Forster, P., Fox-Kemper, B., Fuglestvedt, J., Fyfe, J., Gillett, N., Goldfarb, L., Gorodetskaya, I., Gutierrez, J. M., Hamdi, R., Hawkins, E., Hewitt, H., Hope, P., Islam, A. S., Jones, C., Kaufmann, D., Kopp, R., Kosaka, Y., Kossin, J., Krakovska, S., Li, J., Lee, J.-Y., Masson-Delmotte, V., Mauritsen, T., Maycock, T., Meinshausen, M., Min, S.-k., Ngo Duc, T., Otto, F., Pinto, I., Pirani, A., Raghavan, K., Ranasighe, R., Ruane, A., Ruiz, L., Sallée, J.-B., Samset, B. H., Sathyendranath, S., Monteiro, P. S., Seneviratne, S. I., Sörensson, A. A., Szopa, S., Takayabu, I., Treguier, A.-M., van den Hurk, B., Vautard, R., Von Schuckmann, K., Zaehle, S., Zhang, X., and Zickfeld, K.: Climate Change 2021: The Physical Science Basis. Contribution of Working Group I to the Sixth Assessment Report of the Intergovernmental Panel on Climate Change; Technical Summary, The Intergovernmental Panel on Climate Change AR6, Remote, 2021.

Arola, A., Lipponen, A., Kolmonen, P., Virtanen, T. H., Bellouin, N., Grosvenor, D. P., Gryspeerdt, E., Quaas, J., and Kokkola, H.: Aerosol effects on clouds are concealed by natural cloud heterogeneity and satellite retrieval errors, Nat. Commun., 13, 1-8, https://doi.org/10.1038/s41467-022-34948-5, 2022.

Bangert, M., Kottmeier, C., Vogel, B., and Vogel, H.: Regional scale effects of the aerosol cloud interaction simulated with an online coupled comprehensive chemistry model, Atmos. Chem. Phys., 11, 4411-4423, https://doi.org/10.5194/acp-11-4411-2011, 2011.

Bao, J. W., Feng, J. M., and Wang, Y. L.: Dynamical downscaling simulation and future projection of precipitation over China, Journal of Geophysical Research-Atmospheres, 120, 8227-8243, https://doi.org/10.1002/2015jd023275, 2015.

Brenguier, J.-L., Pawlowska, H., Schüller, L., Preusker, R., Fischer, J., and Fouquart, Y.: Radiative properties of boundary layer clouds: Droplet effective radius versus number concentration, J. Atmos. Sci., 57, 803-821, https://doi.org/10.1175/1520-0469(2000)057<0803:RPOBLC>2.0.CO;2, 2000.

Bretherton, C. S., Blossey, P. N., and Uchida, J.: Cloud droplet sedimentation, entrainment efficiency, and subtropical stratocumulus albedo, Geophys. Res. Lett., 34, https://doi.org/10.1029/2006gl027648, 2007.

Carslaw, K. S., Boucher, O., Spracklen, D. V., Mann, G. W., Rae, J. G. L., Woodward, S., and Kulmala, M.: A review of natural aerosol interactions and feedbacks within the Earth system, Atmos. Chem. Phys., 10, 1701-1737, https://doi.org/10.5194/acp-10-1701-2010, 2010.

Chen, Y. C., Christensen, M. W., Stephens, G. L., and Seinfeld, J. H.: Satellite-based estimate of global aerosol-cloud radiative forcing by marine warm clouds, Nat. Geosci., 7, 643-646, https://doi.org/10.1038/ngeo2214, 2014.

Chen, Y. Y., Yang, K., Zhou, D. G., Qin, J., and Guo, X. F.: Improving the Noah Land Surface Model in Arid Regions with an Appropriate Parameterization of the Thermal Roughness Length, J. Hydrometeorol., 11, 995-1006, https://doi.org/10.1175/2010jhm1185.1, 2010.

Christensen, M. W. and Stephens, G. L.: Microphysical and macrophysical responses of marine stratocumulus polluted by underlying ships: 2. Impacts of haze on precipitating clouds, Journal of Geophysical Research-Atmospheres, 117, https://doi.org/10.1029/2011jd017125, 2012.

Christensen, M. W., Chen, Y. C., and Stephens, G. L.: Aerosol indirect effect dictated by liquid clouds, Journal of Geophysical Research: Atmospheres, 121, 14,636-614,650, https://doi.org/10.1002/2016JD025245, 2016.

Christensen, M. W., Gettelman, A., Cermak, J., Dagan, G., Diamond, M., Douglas, A., Feingold, G., Glassmeier, F., Goren, T., and Grosvenor, D. P.: Opportunistic experiments to constrain aerosol effective radiative forcing, Atmos. Chem. Phys., 22, 641-674, https://doi.org/10.5194/acp-22-641-2022, 2022.

Church, J., Clark, P., Cazenave, A., Gregory, J., and Unnikrishnan, A.: Climate Change 2013: The Physical Science Basis. Contribution of Working Group I to the Fifth Assessment Report of the Intergovernmental Panel on Climate Change, Computational Geometry, https://doi.org/10.1016/S0925-7721(01)00003-7, 2013.

Emmons, L. K., Schwantes, R. H., Orlando, J. J., Tyndall, G., Kinnison, D., Lamarque, J., Marsh, D., Mills, M. J., Tilmes, S.,

and Bardeen, C.: The chemistry mechanism in the community earth system model version 2 (CESM2), J. Adv. Model. Earth Syst., 12, e2019MS001882, https://doi.org/10.1029/2019MS001882, 2020.

Fan, J. W., Leung, L. R., Li, Z. Q., Morrison, H., Chen, H. B., Zhou, Y. Q., Qian, Y., and Wang, Y.: Aerosol impacts on clouds and precipitation in eastern China: Results from bin and bulk microphysics, Journal of Geophysical Research-Atmospheres, 117, https://doi.org/10.1029/2011jd016537, 2012.

Fan, J. W., Liu, Y. C., Xu, K. M., North, K., Collis, S., Dong, X. Q., Zhang, G. J., Chen, Q., Kollias, P., and Ghan, S. J.: Improving representation of convective transport for scale-aware parameterization: 1. Convection and cloud properties simulated with spectral bin and bulk microphysics, Journal of Geophysical Research-Atmospheres, 120, 3485-3509, https://doi.org/10.1002/2014jd022142, 2015.

Fast, J. D., Gustafson, W. I., Easter, R. C., Zaveri, R. A., Barnard, J. C., Chapman, E. G., Grell, G. A., and Peckham, S. E.: Evolution of ozone, particulates, and aerosol direct radiative forcing in the vicinity of Houston using a fully coupled meteorology-chemistry-aerosol model, Journal of Geophysical Research-Atmospheres, 111, https://doi.org/10.1029/2005jd006721, 2006.

Fuentes, E., Coe, H., Green, D., and McFiggans, G.: On the impacts of phytoplankton-derived organic matter on the properties of the primary marine aerosol–Part 2: Composition, hygroscopicity and cloud condensation activity, Atmos. Chem. Phys., 11, 2585-2602, https://doi.org/10.5194/acp-11-2585-2011, 2011.

Gao, W. H., Fan, J. W., Easter, R. C., Yang, Q., Zhao, C., and Ghan, S. J.: Coupling spectral-bin cloud microphysics with the MOSAIC aerosol model in WRF-Chem: Methodology and results for marine stratocumulus clouds, J. Adv. Model. Earth Syst., 8, 1289-1309, https://doi.org/10.1002/2016ms000676, 2016.

Gryspeerdt, E., Goren, T., Sourdeval, O., Quaas, J., Mulmenstadt, J., Dipu, S., Unglaub, C., Gettelman, A., and Christensen, M.: Constraining the aerosol influence on cloud liquid water path, Atmos. Chem. Phys., 19, 5331-5347, https://doi.org/10.5194/acp-19-5331-2019, 2019.

Guenther, A., Karl, T., Harley, P., Wiedinmyer, C., Palmer, P. I., and Geron, C.: Estimates of global terrestrial isoprene emissions using MEGAN (Model of Emissions of Gases and Aerosols from Nature), Atmos. Chem. Phys., 6, 3181-3210, https://doi.org/10.5194/acp-6-3181-2006, 2006.

Hartmann, D. L., Ockert-Bell, M. E., and Michelsen, M. L.: The Effect of Cloud Type on Earth's Energy Balance: Global Analysis, J. Clim., 5, 1281-1304, https://doi.org/10.1175/1520-0442(1992)005<1281:Teocto>2.0.Co;2, 1992.

Heyn, I., Block, K., Mulmenstadt, J., Gryspeerdt, E., Kuhne, P., Salzmann, M., and Quaas, J.: Assessment of simulated aerosol effective radiative forcings in the terrestrial spectrum, Geophys. Res. Lett., 44, 1001-1007, https://doi.org/10.1002/2016gl071975, 2017.

Hu, Y. W., Zang, Z. L., Ma, X. Y., Li, Y., Liang, Y. F., You, W., Pan, X. B., and Li, Z. J.: Four-dimensional variational assimilation for SO2 emission and its application around the COVID-19 lockdown in the spring 2020 over China, Atmos. Chem. Phys., 22, 13183-13200, https://doi.org/10.5194/acp-22-13183-2022, 2022.

Huffman, G. J., Stocker, E. F., Bolvin, D. T., Nelkin, E. J., and Tan, J.: GPM IMERG Final Precipitation L3 1 day 0.1 degree x 0.1 degree V06, Edited by Andrey Savtchenko, Greenbelt, MD [dataset], https://doi.org/10.5067/GPM/IMERGDF/DAY/06, 2019.

Islam, T., Srivastava, P. K., Rico-Ramirez, M. A., Dai, Q., Gupta, M., and Singh, S. K.: Tracking a tropical cyclone through WRF-ARW simulation and sensitivity of model physics, Nat. Hazard., 76, 1473-1495, https://doi.org/10.1007/s11069-014-1494-8, 2015.

Jia, H. L., Ma, X. Y., Quaas, J., Yin, Y., and Qiu, T.: Is positive correlation between cloud droplet effective radius and aerosol optical depth over land due to retrieval artifacts or real physical processes?, Atmos. Chem. Phys., 19, 8879-8896, https://doi.org/10.5194/acp-19-8879-2019, 2019a.

Jia, H. L., Ma, X. Y., and Liu, Y. G.: Exploring aerosol-cloud interaction using VOCALS-REx aircraft measurements, Atmos. Chem. Phys., 19, 7955-7971, https://doi.org/10.5194/acp-19-7955-2019, 2019b.

Khain, A., Pokrovsky, A., Pinsky, M., Seifert, A., and Phillips, V.: Simulation of Effects of Atmospheric Aerosols on Deep Turbulent Convective Clouds Using a Spectral Microphysics Mixed-Phase Cumulus Cloud Model. Part I: Model Description and Possible Applications, J. Atmos. Sci., 61, 2963-2982, https://doi.org/10.1175/jas-3350.1, 2004.

Khain, A., Lynn, B., and Dudhia, J.: Aerosol effects on intensity of landfalling hurricanes as seen from simulations with the WRF model with spectral bin microphysics, J. Atmos. Sci., 67, 365-384, https://doi.org/10.1175/2009JAS3210.1, 2010.

Khain, A. P., Beheng, K. D., Heymsfield, A., Korolev, A., Krichak, S. O., Levin, Z., Pinsky, M., Phillips, V., Prabhakaran, T.,

Teller, A., van den Heever, S. C., and Yano, J. I.: Representation of microphysical processes in cloud-resolving models: Spectral (bin) microphysics versus bulk parameterization, Rev. Geophys., 53, 247-322, https://doi.org/10.1002/2014rg000468, 2015.

Krishna, R. K., Ghude, S. D., Kumar, R., Beig, G., Kulkarni, R., Nivdange, S., and Chate, D.: Surface PM2. 5 estimate using satellite-derived aerosol optical depth over India, Aerosol Air Qual. Res., 19, 25-37, https://doi.org/10.4209/aaqr.2017.12.0568, 2019.

Kumar, R., Barth, M., Pfister, G., Naja, M., and Brasseur, G.: WRF-Chem simulations of a typical pre-monsoon dust storm in northern India: influences on aerosol optical properties and radiation budget, Atmos. Chem. Phys., 14, 2431-2446, https://doi.org/10.5194/acp-14-2431-2014, 2014.

Lebo, Z. J., Morrison, H., and Seinfeld, J. H.: Are simulated aerosol-induced effects on deep convective clouds strongly dependent on saturation adjustment?, Atmos. Chem. Phys., 12, 9941-9964, https://doi.org/10.5194/acp-12-9941-2012, 2012.

Levy, R., Hsu, C., ~~and~~ et, a~~l~~.: MODIS Atmosphere L2 Aerosol Product. NASA MODIS Adaptive Processing System, Goddard Space Flight Center, USA [dataset], https://doi.org/10.5067/MODIS/MOD04_L2.061, 2015.

Li, G. H., Wang, Y., and Zhang, R. Y.: Implementation of a two-moment bulk microphysics scheme to the WRF model to investigate aerosol-cloud interaction, Journal of Geophysical Research-Atmospheres, 113, https://doi.org/10.1029/2007jd009361, 2008.

Li, X. S., Choi, Y., Czader, B., Roy, A., Kim, H., Lefer, B., and Pan, S.: The impact of observation nudging on simulated meteorology and ozone concentrations during DISCOVER-AQ 2013 Texas campaign, Atmos. Chem. Phys., 16, 3127-3144, https://doi.org/10.5194/acp-16-3127-2016, 2016.

Liu, Y., Bourgeois, A., Warner, T., Swerdlin, S., and Hacker, J.: Implementation of observation-nudging based FDDA into WRF for supporting ATEC test operations, WRF/MM5 Users' Workshop June, 27-30,

Maussion, F., Scherer, D., Finkelnburg, R., Richters, J., Yang, W., and Yao, T.: WRF simulation of a precipitation event over the Tibetan Plateau, China - an assessment using remote sensing and ground observations, Hydrol. Earth Syst. Sci., 15, 1795-1817, https://doi.org/10.5194/hess-15-1795-2011, 2011.

Michibata, T., Suzuki, K., Sato, Y., and Takemura, T.: The source of discrepancies in aerosol-cloud-precipitation interactions between GCM and A-Train retrievals, Atmos. Chem. Phys., 16, 15413-15424, https://doi.org/10.5194/acp-16-15413-2016, 2016.

Mlawer, E. J., Taubman, S. J., Brown, P. D., Iacono, M. J., and Clough, S. A.: Radiative transfer for inhomogeneous atmospheres: RRTM, a validated correlated-k model for the longwave, J. Geophys. Res.: Atmos., 102, 16663-16682, https://doi.org/https://doi.org/10.1029/97JD00237, 1997.

Mulmenstadt, J. and Feingold, G.: The Radiative Forcing of Aerosol-Cloud Interactions in Liquid Clouds: Wrestling and Embracing Uncertainty, Curr. Clim. Change Rep., 4, 23-40, https://doi.org/10.1007/s40641-018-0089-y, 2018.

Ngan, F. and Stein, A. F.: A Long-Term WRF Meteorological Archive for Dispersion Simulations: Application to Controlled Tracer Experiments, Journal of Applied Meteorology and Climatology, 56, 2203-2220, https://doi.org/10.1175/jamc-d-16-0345.1, 2017.

Niu, X., Ma, X., and Jia, H.: Analysis of cloud-type distribution characteristics over major aerosol emission regions in the Northern Hemisphere by using CloudSat/CALIPSO satellite data, Journal of the Meteorological Sciences, 42, 467-480, https://doi.org/10.12306/2021jms.0006, 2022.

Pahlow, M., Parlange, M. B., and Porté-Agel, F.: On Monin–Obukhov similarity in the stable atmospheric boundary layer, Boundary Layer Meteorol., 99, 225-248, https://doi.org/10.1023/A:1018909000098, 2001.

Platnick, S., Ackerman, S., ~~and~~ King, M., et al.: MODIS Atmosphere L2 Cloud Product (06_L2). NASA MODIS Adaptive Processing System, Goddard Space Flight Center, USA [dataset], https://doi.org/10.5067/MODIS/MOD06_L2.061, 2015.

Quaas, J., Boucher, O., and Lohmann, U.: Constraining the total aerosol indirect effect in the LMDZ and ECHAM4 GCMs using MODIS satellite data, Atmos. Chem. Phys., 6, 947-955, https://doi.org/10.5194/acp-6-947-2006, 2006.

Quaas, J., Boucher, O., Jones, A., Weedon, G. P., Kieser, J., and Joos, H.: Exploiting the weekly cycle as observed over Europe to analyse aerosol indirect effects in two climate models, Atmos. Chem. Phys., 9, 8493-8501, https://doi.org/10.5194/acp-9-8493-2009, 2009.

Quaas, J., Arola, A., Cairns, B., Christensen, M., Deneke, H., Ekman, A. M. L., Feingold, G., Fridlind, A., Gryspeerdt, E., Hasekamp, O., Li, Z. Q., Lipponen, A., Ma, P. L., Mulmenstadt, J., Nenes, A., Penner, J. E., Rosenfeld, D., Schrodner,

860 R., Sinclair, K., Sourdeval, O., Stier, P., Tesche, M., van Diedenhoven, B., and Wendisch, M.: Constraining the Twomey effect from satellite observations: issues and perspectives, Atmos. Chem. Phys., 20, 15079-15099, https://doi.org/10.5194/acp-20-15079-2020, 2020.

Rogers, R. E., Deng, A. J., Stauffer, D. R., Gaudet, B. J., Jia, Y. Q., Soong, S. T., and Tanrikulu, S.: Application of the Weather Research and Forecasting Model for Air Quality Modeling in the San Francisco Bay Area, Journal of Applied Meteorology and Climatology, 52, 1953-1973, https://doi.org/10.1175/jamc-d-12-0280.1, 2013.

865 Roh, W., Satoh, M., Hashino, T., Okamoto, H., and Seiki, T.: Evaluations of the thermodynamic phases of clouds in a cloud-system-resolving model using CALIPSO and a satellite simulator over the Southern Ocean, J. Atmos. Sci., 77, 3781-3801, https://doi.org/10.1175/JAS-D-19-0273.1, 2020.

Rosenfeld, D., Zhu, Y. N., Wang, M. H., Zheng, Y. T., Goren, T., and Yu, S. C.: Aerosol-driven droplet concentrations dominate coverage and water of oceanic low-level clouds, Science, 363, 599-+, https://doi.org/10.1126/science.aav0566, 870 2019.

Saponaro, G., Kolmonen, P., Sogacheva, L., Rodriguez, E., Virtanen, T., and de Leeuw, G.: Estimates of the aerosol indirect effect over the Baltic Sea region derived from 12 years of MODIS observations, Atmos. Chem. Phys., 17, 3133-3143, https://doi.org/10.5194/acp-17-3133-2017, 2017.

Sha, T., Ma, X. Y., Jia, H. L., Tian, R., Chang, Y. H., Cao, F., and Zhang, Y. L.: Aerosol chemical component: Simulations 875 with WRF-Chem and comparison with observations in Nanjing, Atmos. Environ., 218, https://doi.org/10.1016/j.atmosenv.2019.116982, 2019.

Sha, T., Ma, X. Y., Wang, J., Tian, R., Zhao, J. Q., Cao, F., and Zhang, Y. L.: Improvement of inorganic aerosol component in $PM_{2.5}$ by constraining aqueous-phase formation of sulfate in cloud with satellite retrievals: WRF-Chem simulations, Sci. Total Environ., 804, https://doi.org/10.1016/j.scitotenv.2021.150229, 2022.

880 Shin, H. H., Hong, S. Y., and Dudhia, J.: Impacts of the Lowest Model Level Height on the Performance of Planetary Boundary Layer Parameterizations, Mon. Weather Rev., 140, 664-682, https://doi.org/10.1175/mwr-d-11-00027.1, 2012.

Sicard, P., Crippa, P., De Marco, A., Castruccio, S., Giani, P., Cuesta, J., Paoletti, E., Feng, Z. Z., and Anav, A.: High spatial resolution WRF-Chem model over Asia: Physics and chemistry evaluation, Atmos. Environ., 244, https://doi.org/10.1016/j.atmosenv.2020.118004, 2021.

885 Small, J. D., Chuang, P. Y., Feingold, G., and Jiang, H. L.: Can aerosol decrease cloud lifetime?, Geophys. Res. Lett., 36, https://doi.org/10.1029/2009gl038888, 2009.

Soni, P., Tripathi, S. N., and Srivastava, R.: Radiative effects of black carbon aerosols on Indian monsoon: a study using WRF-Chem model, Theor. Appl. Climatol., 132, 115-134, https://doi.org/10.1007/s00704-017-2057-1, 2018.

Tian, R., Ma, X. Y., and Zhao, J. Q.: A revised mineral dust emission scheme in GEOS-Chem: improvements in dust 890 simulations over China, Atmos. Chem. Phys., 21, 4319-4337, https://doi.org/10.5194/acp-21-4319-2021, 2021.

Toll, V., Christensen, M., Quaas, J., and Bellouin, N.: Weak average liquid-cloud-water response to anthropogenic aerosols, Nature, 572, 51-55, https://doi.org/10.1038/s41586-019-1423-9, 2019.

Tuccella, P., Curci, G., Visconti, G., Bessagnet, B., Menut, L., and Park, R. J.: Modeling of gas and aerosol with WRF/Chem over Europe: Evaluation and sensitivity study, Journal of Geophysical Research-Atmospheres, 117, 895 https://doi.org/10.1029/2011jd016302, 2012.

Twomey, S.: The Influence of Pollution on the Shortwave Albedo of Clouds, Journal of Atmospheric Sciences, 34, 1149-1152, https://doi.org/10.1175/1520-0469(1977)034<1149:Tiopot>2.0.Co;2, 1977.

Wang, F., Guo, J. P., Zhang, J. H., Huang, J. F., Min, M., Chen, T. M., Liu, H., Deng, M. J., and Li, X. W.: Multi-sensor quantification of aerosol-induced variability in warm clouds over eastern China, Atmos. Environ., 113, 1-9, 900 https://doi.org/10.1016/j.atmosenv.2015.04.063, 2015.

Wang, Y., Fan, J. W., Zhang, R. Y., Leung, L. R., and Franklin, C.: Improving bulk microphysics parameterizations in simulations of aerosol effects, Journal of Geophysical Research-Atmospheres, 118, 5361-5379, https://doi.org/10.1002/jgrd.50432, 2013.

Wilcox, L. J., Highwood, E. J., and Dunstone, N. J.: The influence of anthropogenic aerosol on multi-decadal variations of 905 historical global climate, Environ. Res. Lett., 8, https://doi.org/10.1088/1748-9326/8/2/024033, 2013.

Wild, O., Zhu, X., and Prather, M. J.: Fast-J: Accurate simulation of in-and below-cloud photolysis in tropospheric chemical models, J. Atmos. Chem., 37, 245-282, https://doi.org/10.1023/A:1006415919030, 2000.

Xu, W. F., Liu, P., Cheng, L., Zhou, Y., Xia, Q., Gong, Y., and Liu, Y. N.: Multi-step wind speed prediction by combining a

WRF simulation and an error correction strategy, Renewable Energy, 163, 772-782, https://doi.org/10.1016/j.renene.2020.09.032, 2021.

Zaveri, R. A., Easter, R. C., Fast, J. D., and Peters, L. K.: Model for Simulating Aerosol Interactions and Chemistry (MOSAIC), Journal of Geophysical Research-Atmospheres, 113, https://doi.org/10.1029/2007jd008782, 2008.

Zhang, X., Wang, H., Che, H. Z., Tan, S. C., Yao, X. P., Peng, Y., and Shi, G. Y.: Radiative forcing of the aerosol-cloud interaction in seriously polluted East China and East China Sea, Atmos. Res., 252, https://doi.org/10.1016/j.atmosres.2020.105405, 2021a.

Zhang, Y. W., Fan, J. W., Li, Z. Q., and Rosenfeld, D.: Impacts of cloud microphysics parameterizations on simulated aerosol–cloud interactions for deep convective clouds over Houston, Atmos. Chem. Phys., 21, 2363-2381, https://doi.org/10.5194/acp-21-2363-2021, 2021b.

Zhang, Z. B., Ackerman, A. S., Feingold, G., Platnick, S., Pincus, R., and Xue, H. W.: Effects of cloud horizontal inhomogeneity and drizzle on remote sensing of cloud droplet effective radius: Case studies based on large-eddy simulations, Journal of Geophysical Research-Atmospheres, 117, https://doi.org/10.1029/2012jd017655, 2012.

Zhao, C., Liu, X., Leung, L. R., Johnson, B., McFarlane, S. A., Gustafson, W. I., Fast, J. D., and Easter, R.: The spatial distribution of mineral dust and its shortwave radiative forcing over North Africa: modeling sensitivities to dust emissions and aerosol size treatments, Atmos. Chem. Phys., 10, 8821-8838, https://doi.org/10.5194/acp-10-8821-2010, 2010.

Zhao, J. Q., Ma, X. Y., Wu, S. Q., and Sha, T.: Dust emission and transport in Northwest China: WRF-Chem simulation and comparisons with multi-sensor observations, Atmos. Res., 241, https://doi.org/10.1016/j.atmosres.2020.104978, 2020.

Zhong, X. h., Ruiz-Arias, J. A., and Kleissl, J.: Dissecting surface clear sky irradiance bias in numerical weather prediction: Application and corrections to the New Goddard Shortwave Scheme, Sol. Energy, 132, 103-113, https://doi.org/10.1016/j.solener.2016.03.009, 2016.

Zhou, C. and Penner, J. E.: Why do general circulation models overestimate the aerosol cloud lifetime effect? A case study comparing CAM5 and a CRM, Atmos. Chem. Phys., 17, 21-29, https://doi.org/10.5194/acp-17-21-2017, 2017.